The Pennsylvania State University
The Graduate School
College of Engineering

A COMPARISON OF MODELING APPROACHES OF A HIGH ASPECT CYLINDER IN AXIAL FLOW

A Thesis in
Engineering Science and Mechanics
by
Nicholas LaBarbera

Submitted in Partial Fulfillment
of the Requirements
for the Degree of

Master of Science

December 2015

The thesis of Nicholas LaBarbera was reviewed and approved* by the following:

Jonathan S. Pitt
Research Associate, Applied Research Laboratory
Assistant Professor of Engineering Science and Mechanics
Thesis Advisor

Robert L. Campbell
Research Associate, Applied Research Laboratory
Assistant Professor of Mechanical Engineering

Judith A. Todd
P.B. Breneman Department Chair
Department of Engineering Science and Mechanics

*Signatures are on file in the Graduate School.

Abstract

Simulating a fully-coupled fluid-structure interaction system from first-principles can be very computationally expensive especially for use in design-level analyses; therefore, it is advantageous to explore less computationally expensive methods. By making assumptions about the relevant physics of the problem, simplifications to the governing equations can be applied. These simplifications result in a reduced-order model that can significantly decrease the computational cost; however, the governing equations simplifications result in the reduced-order model neglecting to take into account all the physics of the system. Ideally, the neglected physics would have little to no impact on the dynamics of the system; however, this is not always the case for all input parameters. Therefore, it is important to determine the parameter space for which a reduced order model is valid.

In this thesis, numerical simulations of a slender cylinder in axial flow were performed using two different methods. The first is a strongly-coupled fluid-structure interaction simulation based on first-principles. First-principles for this case is solving the incompressible Navier-Stokes equations for the fluid and the full equations of elasticity for the solid domain. The second is a reduced-order model for a cylinder in axial flow that was devised by Paidoussis. It consists of a single linear partial differential equation that requires significantly less computational resources to solve than the non-linear governing equations used in the first-principles model. For certain input parameters, the reduced-order model is capable of predicting stability with comparable accuracy to the first-principles model, but is obtained in a fraction of the time.

The goal of this thesis is to investigate the parameter space for which the less computational expensive reduced order model can be utilized and for which the more computationally expensive first-principles solver is required. To accomplish the goal, the two models were compared through the variation of input parameters to determine the parameter ranges corresponding to agreement between models. Results are presented and conclusions discussed.

Table of Contents

List of Figures

List of Tables

List of Symbols

E	Young's Modulus
I	Moment of Inertia
U	Free-stream speed of the fluid
D	Diameter of the cylinder
L	Length of the cylinder
m	mass per unit length of the cylinder
M	Mass of the displaced fluid
c_t	Longitudinal drag coefficient
c_n	Normal drag coefficient
c_2	Base drag coefficient
f	Measure of tail piece slenderness
l	Length of tail piece
t	time
ρ	density
p	pressure
μ	viscosity
$\mathbf{u}$	fluid velocity vector

$\mathbf{u}^m$	mesh velocity
$\mathbf{S}$	Second Piola-Kirchhoff stress
$\mathbf{E}$	Lagrangian Green strain
λ	Lame Constant
y	Displacement of the cylinder
w	Slope of the cylinder
u	Curvature of the cylinder
v	velocity of the cylinder

Acknowledgments

I would like to acknowledge Naval Sea Systems Command Advanced Submarines Systems Development Office (SEA 073R) and the Penn State Applied Research Laboratory for funding to conduct this research. I also owe a major thanks to Dr. Jonathan Pitt & Dr. Scott Miller for advising during this research. Without their help and guidance, this thesis wouldn't have been possible. Finally, I would like to thank my family for encouraging me to go back to school to pursue a graduate degree.

Chapter 1
Introduction

1.1 Introduction

Computational mechanics has played an important role in the engineering design process over the past few decades by providing the necessary tools to go from a mathematical model of a complex system to its predicted behavior. The role of computational mechanics is likely to only expand as advancements continue to be made in both software and hardware.

Increases in computational resource availability have made it possible to simulate problems and phenomenon that were once too computationally expensive. In particular, the demand for coupled multi-physics simulations has been increasing over the years. A multi-physics simulation couples different physical models into a single model. An example would be coupling thermal effects with a structure's mechanical response.

This thesis focuses on the specific multi-physics problem of fluid-structure interaction (FSI). A fluid-structure interaction simulation couples the governing equations of solid mechanics with the governing equations of fluid mechanics. Fluid-structure interaction is characterized by the interaction of a deformable solid whose deformation is dependent on the fluid's flow field and a fluid whose flow field is dependent on the solid's deformation. It is this two-way coupling that exemplifies the multi-physics nature of a fluid-structure interaction problem.

The physical world is full of examples of fluid-structure interaction such as a tree branch swaying in a breeze or a fish swimming in a stream. There are also fluid-structure interaction problems of practical engineering interest such as the

deformation of wind turbine blades (Bazilevs et al., 2011) and the simulation of artificial heart valves (Dumont et al., 2007).

This thesis will focus on the particular fluid-structure interaction problem of a slender cylinder in axial flow. It has garnered interest from the research community due to its application to heat exchangers, nuclear reactor fuel-element bundles and acoustic streamers (Paidoussis, 2004). A cylinder in axial flow may experience vibrations, due to shedding vortices impinging on the cylinder downstream, causing self-excitation. It is important for engineers to recognize the potential effects of these vibrations especially in closely spaced systems. One scenario where axial flow induced vibrations must be considered is in the design of closely spaced nuclear cooling rods. If the vibrations are not considered during the design phase, the spacing might be too small and the rods could collide during vibrations (Liu et al., 2012). This can result in fretting and long term problems such as fatigue and stress-corrosion cracking (Paidoussis, 2004). Fluid-structure interaction simulations modelled with first-principal approaches can accurately capture the physics of a system; however, this accuracy comes at a price. It requires solving the full Navier-Stokes equations for the fluid domain and the equations of elasticity for the solid domain. The result is a very large set of equations that must be solved each time step; requiring significant computational resources and time. Thus, it is advantageous to explore less computationally expensive methods. By making assumptions about the relevant physics of the problem, simplifications to the governing equations can be applied. These simplifications result in a reduced-order model of the system that can significantly decrease the computational cost.

Reduced-order model simulations can run orders of magnitude faster, but by not basing a model on first-principles, some of the physics are lost and their effects are not captured. In certain situations, these neglected physics can play a significant role and result in the reduced-order model producing inaccurate results. In other situations, the physics neglected by the reduced-order model can be of little significance. In these situations, the reduced-order model can produce accurate predictions but in a fraction of the time.

This thesis starts with a literature review of current modelling efforts for towed arrays and cylinders in axial flow. Next, the Paidoussis reduced order model is discussed and its implementation into a finite element solver. After that section, the details on the first principles solver are presented. This is followed by a chapter

outlining how the comparison cases are set up and results from the simulations. Finally, conclusions are discussed and directions for future work and research are provided. This is outlined in Figure 1.1.

The goal of this research is to investigate the parameter space that the reduced-order model provides accurate stability predictions and which parameter space is the more computationally expensive first-principals model necessary. To do this, a first principles fluid-structure interaction solver was compared to the Paidoussis reduced-order model for a cylinder in axial flow.

The first principles fluid-structure interaction solver used for comparison is an in-house partitioned solver. A partitioned solver uses seperate solves for the fluid and structural domains. To solve the fluid, the open-source finite-volume solver, OpenFOAM (Jasak, 1996) version 2.2 was used. For the fluid, the incompressible Navier-Stokes equations are solved. The equations of elasticity for a hyper-elastic solid are solved using an in-house finite element solver, FEANL (Campbell, 2011). The two domains are coupled using an in-house coupling code.

The reduced-order model implemented is the Paidoussis model (Paidoussis, 1973) for a cylinder in axial flow. The governing equation for the Paidoussis model is linear, and therefore requires much less computational resources to solve numerically. This speed increase comes at the cost of lost physics. One effect not modeled is the effect of the cylinder's deformation on the flow field of the fluid. Also effects such as vortex shedding are neglected. A thorough treatment on the Paidoussis model as well the dynamics of structures in axial flow can be found in (Paidoussis, 2004). The Paidoussis model was numerically implemented for the test case using the open-source finite element library Deal.ii (Bangerth et al., 2013). A case for comparison was simulated using both approaches and compared to determine the range of validity for the reduced-order model.

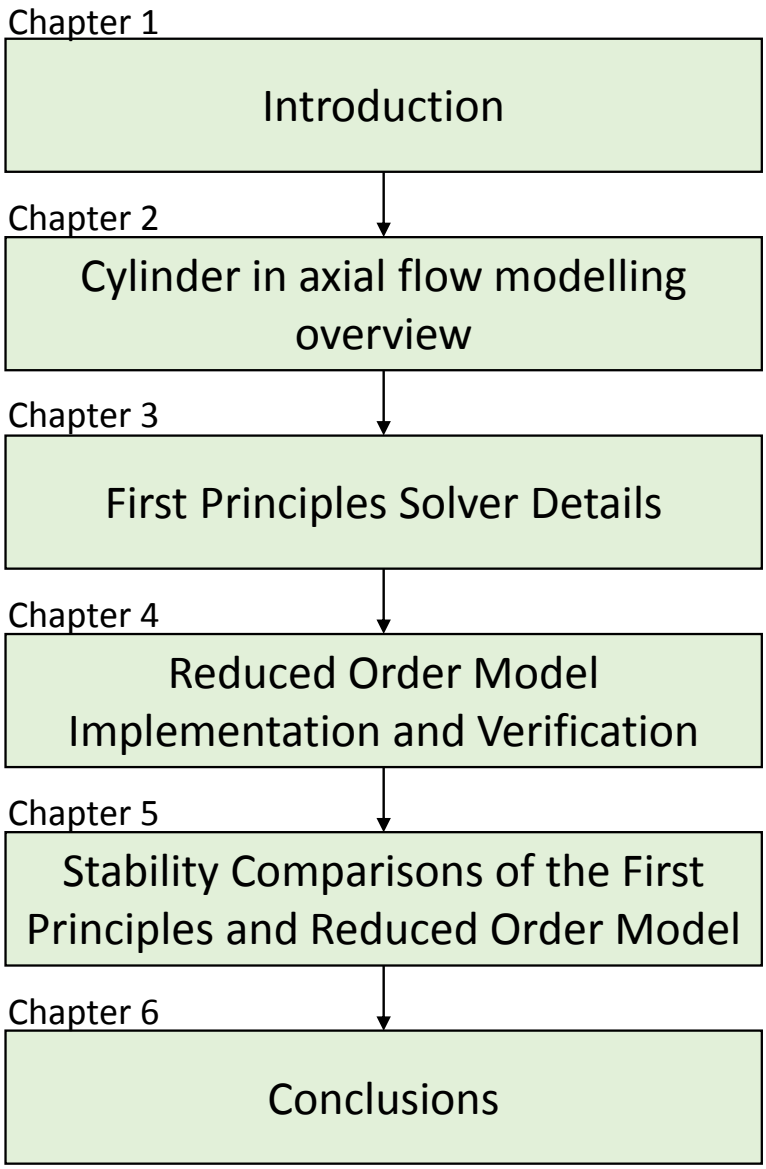

Figure 1.1: A flow chart outlining the work presented in this thesis.

Chapter 2
Literature Review

2.1 Introduction

Sonar has found many uses in the world. It can be used to map the seabed for navigational safety maps and cable-laying routes. The oil-industry uses sonar to to explore for potential drill sites and sonar has long been a standard tool used by the Navy for target detection (Lemon, 2004). In all these applications, it is beneficial to have the maximum resolution and range possible. This has lead to the development of towed sonar-array systems or towed arrays for short.

Towed arrays have superior range and resolution in comparison to hull mounted sonars; however, the effectiveness of a towed array is directly proportional to how precise the instantaneous location of each individual hydrophone on the array is known (Gerstoft et al., 2003). Therefore, there exists a need to be able to accurately predict the shape of an array under various operating conditions. Towed arrays can be several kilometers long, which makes performing full-scale experiments an extremely difficult task. Due to the high aspect-ratio of towed arrays, it is difficult to perform scaled model experiments. Thus, computer simulations are the most feasible option for predicting array shape and motion.

A towed array is a long, slender cable that is towed hundreds of meters behind a ship. Hydrophones are attached to the cable sufficiently far away from the ship to reduce the amount of noise picked up from the ship itself (Barbagelata et al., 2008). The sensor array is typically 2 to 4 inches in diameter and towed by a cable up to 8,000 ft long (Pike, 2013; Lasky et al., 2004). A drawing of a towed array is shown in Figure 2.1. Inside the array are wires to carry data and electricity, hydrophones

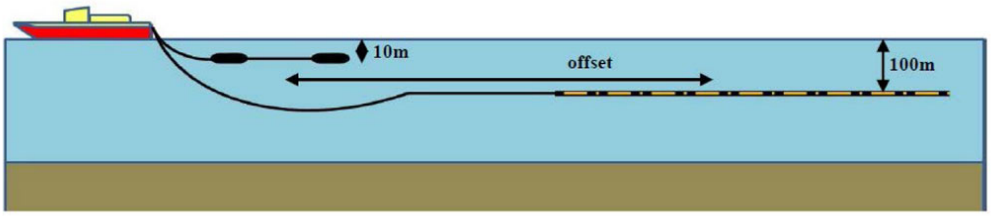

Figure 2.1: A typical towed array (Zhdanov, 2013)

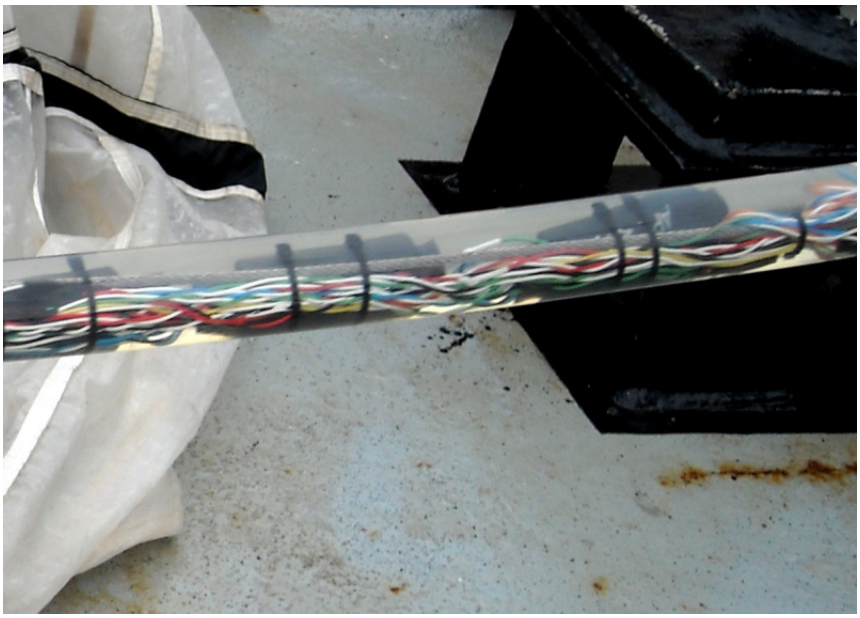

Figure 2.2: Close up of oil filled towed array used for marine biology research (Gogan, 2014)

to pick up sounds, and oil to make the array neutrally buoyant and to help dissipate heat from the electrical equipment (Pike, 2013; Lasky et al., 2004). This is shown in Figure 2.2. A drogue will sometimes be attached to increase tension and stability in the line.

Towed arrays come in different lengths and numbers depending on their intended use. The oil exploration field will tow up to 16 arrays at once from a single ship (Lemon, 2004). A few dimensions for towed arrays used for oceanography research are presented below in Table 2.1.

Table 2.1: Details of the Prakla Series of Towed Arrays (Barbagelata et al., 2008)

Parameter	Prakla 128	Prakla 256
Year Introduced	1979	1991
Array Length	45 m	254 m
Hose Diameter	68 mm	90 mm
Tow cable length	1000 m	1500 m
Tow cable diameter	62 mm	25.4 mm
Number of Hydrophones	64	128

There are several advantages of a towed array sonar system over a hull mounted sonar. The first advantage is the reduction in interference noise picked up by the array. Ships are inherently noisy due to vibrations of the engines, the movement of the propellers, and the crashing of waves on the hull. By having the hydrophones of the array located sufficiently far away from the towing vessel, the towed array picks up less interference noise. Thus, the resolution and range of the towed array is increased over similar hull mounted sonars (Kopp, 2010). Towed Arrays can also be positioned at various depths, which gives towed arrays the ability to take advantage of ocean conditions with better acoustic properties (Barbagelata et al., 2008).

Another advantage of a towed array is its ability to cover the baffles (Lemon, 2004). A baffle is the hull-mounted sonar's blind spot located directly behind the ship. This blind spot is due to the sonar's ineffectiveness in that region from to the noise created by the engine and the propeller (Kopp, 2010).

Perhaps the greatest benefit of a towed array is the ability to utilize the technique of beamforming. Beamforming allows the numerous hydrophones to work together to improve gain as well as resolution (Kopp, 2010). However, beamforming requires that the position of each hydrophone on the array be known, and uncertainty in position results in decreased performance (Barbagelata et al., 2008). One way of handling the uncertainty in the shape of the array is to consider the array as always being in a straight line (Lu et al., 2003), but ocean currents and maneuvering by the towing ship can cause the shape of the array to deviate from being linear (Lu et al., 2003). The uncertainty in the sensor's position reduces the effectiveness

of beamforming, and thus degrades the performance of the array (Gerstoft et al., 2003). There exists a need for the ability to accurately predict an array's shape under various conditions.

There are other disadvantages to using a towed array besides the requirement of knowing the array's shape. The long length and heavy weight of a towed array system results in towed arrays requiring large dedicated machinery for their deployment and retrieval. This is especially a problem for towed array deployment from vessels where space is limited (Potter et al., 2000). A smaller array diameter would be lighter and would require smaller machinery for deployment (Barbagelata et al., 2008), but it is difficult to decrease an array's diameter due to the need for wires to deliver power and transfer data (Pike, 2013). Complicated telemetry schemes for the internal wiring has been used as a means to reduce the array's diameter, but has resulted in higher manufacturing costs and reduced reliability of the array (Pike, 2013). The reduction in reliability furthers the need to be able to accurately predict stresses experienced by the array in various situations.

Another drawback to most single towed arrays is the inability to discern a signal's direction. This is because the hydrophones used for towed arrays are omnidirectional (Lemon, 2004). This problem has been addressed by using two towed arrays, a right and a left array, to discern directivity (Lemon, 2004). Incorporating roll sensors in the towed array or using hydrophone triplets are alternative methods used for discerning directivity (Barbagelata et al., 2008).

Modeling Challenges

Accurately modeling a towed array poses several technical challenges. For example, the aspect ratio for the TB-16 array is roughly 1000:1 (Pike, 2013), and this is without factoring in the length from the tow cable. The large aspect ratio and length of a towed array makes it difficult to perform experiments to validate simulations (Ni, 1978; Srivastava, 1998; Obligado, 2013). It also presents problems for building scale models to be tested in water tunnels and flumes. After scaling the length down to a size that can be tested in a water tunnel, the diameter becomes much too small for accurate scale testing.

A towed array is comprised of different sections made up of different materials with different properties, which further adds complexity to the problem. Further-

more, towed arrays have low bending stiffness which allows them to experience large deviations from a linear configuration.

During maneuvering the flow is not strictly axial flow. Towed arrays experience a cross flow component as well, and the amount of axial and cross flow can vary along the length of the array. Cross flow over a cylinder causes vortex shedding at an increased rate in comparison to axial flow. It is important, and difficult, to determine to what degree the array is experiencing cross flow and axial flow, for both self-noise and dynamic analysis.

Natural conditions such as ocean currents and the heaving of the ship by waves add stochastic components to the model, while ocean currents add even more difficulty by varying along the length of the array. These factors all contribute to the complexity of the system.

2.2 Existing Models

Paidoussis Model

Research on slender and flexible towed bodies began in the 1950's when W.R. Hawthorne invented the Dracone Barge (Paidoussis, 2004). The Dracone Barge is a long flexible tube used to transport lighter than water liquids (Hawthorne, 1961). The modern Dracone Barge is mainly used to aid in cleaning up oil spills by being a container that oil is pumped into (Paidoussis, 2004).

Paidoussis, a former graduate student of Hawthorne, built upon Hawthorne's work and published an analysis of the equations of motion as well as experimental results for a fully submerged cylinder in axial flow (Paidoussis, 1968). His model is often referred to as the "Paidoussis model" or the "Paidoussis equation" (Paidoussis, 2004). The equation is a combination of the inviscid forces derived by Lighthill (1960) during his study on the swimming of fish and the viscous forces derived by Paidoussis (1968). However, Paidoussis' 1968 paper contained an error in the calculation of the viscous forces and was corrected in his 1970 paper. The incorrect 1968 equation will still produce accurate results for short cylinders in axial flow (Paidoussis, 2004).

The corrected 1970 equation for a uniform cylinder in 2D axial flow is

$$EI\frac{\partial^4 y}{\partial x^4} + M(\frac{\partial}{\partial t} + U\frac{\partial}{\partial x})^2 y + \frac{1}{2}c_N\left(\frac{MU}{D}\right)\left(\frac{\partial y}{\partial t} + U\frac{\partial y}{\partial x}\right) - \frac{1}{2}MU^2\left[c_2 + c_T\frac{L-x}{D}\right]\frac{\partial^2 y}{\partial x^2} + m\frac{\partial^2 y}{\partial t^2} = 0 \quad (2.1)$$

where

- EI is the flexural rigidity.
- U is the speed of the fluid.
- D is the diameter of the cylinder.
- L is the length of the cylinder.
- m is the mass per unit length of the cylinder.
- M is the mass of the displaced fluid.
- c_t and c_n are the longitudinal and normal drag coefficients, respectively. They are typically on the order of magnitude of 0.01. Also the ratio, c_n/c_t usually ranges between 0.5 for a rough cylinder and 1.5 for a smooth cylinder (De Langre et al., 2007).
- c_2 is the base drag coefficient which is typically between 0.1 and 0.7 (Paidoussis, 2004). A table of base drag coefficients for various shapes can be found in chapter 10 of (Blevins, 1984).

2.2.1 String Approximation

Given the large aspect ratio of towed arrays, it may be a reasonable approximation to assume there are no internal flexural forces by modeling a towed array as a string (Paidoussis, 2004). This has been investigated by Dowling (1988) and Traintafyllou (1989).

When very long cylinders in axial flow are undergoing vibratory response, there is a neutral point where the tension caused by drag is equal to the inertial forces (De Langre et al., 2007). Upstream of the neutral point, the cylinder is in tension, but the cylinder is in compression downstream of the neutral point. The neutral

point causes a mathematical singularity to arise. This mathematical singularity does not arise when using a string model for cylinders shorter than their neutral point because the entire cylinder is in tension and there are no points of zero stiffness. Dowling overcame the neutral point phenomenon by using asymptotic expansions (Dowling, 1988). M.A. Vaz (1995) used this formulation to model a towed array as a string broken into segments to investigate the transient behaviour of a towed array. The results were compared to the full-scale experiments on cable laying by Hopland (1993) .

Ni & Hansen (1978) conducted experiments for neutrally-buoyant, long, slender cylinders in axial flow. Their results were not in accordance with the string-model predictions of Traintafyllou & Chryssostomidis (1989). However, Paidoussis (2004) comments that if you consider the upstream part of the cylinder as rigid due to tension, then the flexible portion of the cylinder is shorter. The result is a different ratio of length to diameter for the flexible portion and can explain the discrepancies between the experimental observations of Ni & Hansen and the theoretical predictions of Traintafyllou & Chryssostomidis (Paidoussis, 2004). De Langre (2007) builds upon this by going into more detail on modeling a long cylinder as rigid until a critical length. His model treats the the portion of the cylinder before the critical length as rigid and the remaining portion as flexible. He models the flexible downstream portion with a simple string model.

An example of a string equation from G.S. Traintafyllou (1989) is displayed below.

$$[MU^2 - T_0 - \frac{1}{2}\rho DU^2 C_f(L-x)]\frac{\partial^2 y}{\partial x^2} + 2MU\frac{\partial^2 y}{\partial x \partial t} + \frac{1}{2}\rho DUC_f\left(\frac{\partial y}{\partial t} + U\frac{\partial y}{\partial x}\right) + (m+M)\frac{\partial^2 y}{\partial t^2} = 0 \quad (2.2)$$

2.2.2 Beam Modelling

To include flexural forces in a towed array model, the towed array must be modelled as a beam. A beam model overcomes the mathematical difficulties encountered by string models at points of zero tension. This advantage is offset by making the numerical model more computational expensive. The reduced order model implemented in this thesis falls into the category of a linear beam model. These

models are still considered only 1-way coupled because they do not take into account the effect the solid's deformation has on the fluid. Some of the models do use empirical relations to account for the solid's effect on fluid, such as was done by H.I. Park (2003). Park's model incorporated drag coefficients that increased with Reynolds number to take into account vortex shedding.

An example of a governing equation for a cylinder in axial flow modeled using a beam is below (Chen, 1970).

$$EI\frac{\partial^4 y}{\partial x^4} + \rho A U^2 + \frac{1}{4}C_T \rho U^2 L D\frac{\partial^2 y}{\partial x^2} + \frac{1}{2}C_N \rho D\frac{\partial y}{\partial t}(m_\rho A)\frac{\partial^2 y}{\partial t^2} = 0 \qquad (2.3)$$

A subcategory of beam models is cable models. Cable models take into account bending stiffness, as all beam models do, but instead of having the mass continuously distributed, it is instead approximated by a network a lumped masses connected by massless connections (Gobat, 2006). This is shown in Figure 2.3. Each mass is a rigid body with both rotational and translational degrees of freedom. The result of making this approximation is the ability to apply the Newton-Euler equations of motion for each individual mass to obtain a system of equations without the appearance spatial derivatives. The connecting sections are modelled as a collection of massless linear and torsion spring/damper systems to account for stretching and torsional forces in the cable (Gobat, 2006). Furthermore, it is possible to model anisotropic materials by modeling the system as a set of spring/damper systems in different planes with different properties (Orcina, 2013). By adding additional modeling to the system, cable models can simulate things such as contact and hysteresis.

The advantage of cable models are that they are more efficient than solving the full elasticity equations. Time-savings are also reaped by decoupling the solid's effect on the fluid's flow field. The price of these speed increases is a loss of accuracy when compared to a fully-coupled simulation that solves the elasticity equations and the Navier-Stokes equations. It is worth noting that cable models still only have one-way coupling. Specifically, the fluid's effect on the solid is taken into account, but the solid's effect on the fluid is ignored. Cable models also do not directly model some fluid phenomenon such as vortices being shed by the cable. Therefore, a cable model is not a fully-coupled first principles model for a towed array. Examples of cable models already developed are the Wood's Hole Oceanic

Institute (WHOI) CABLE program (Gobat, 1998) and the commercial program OrcaFlex (Orcina, 2013).

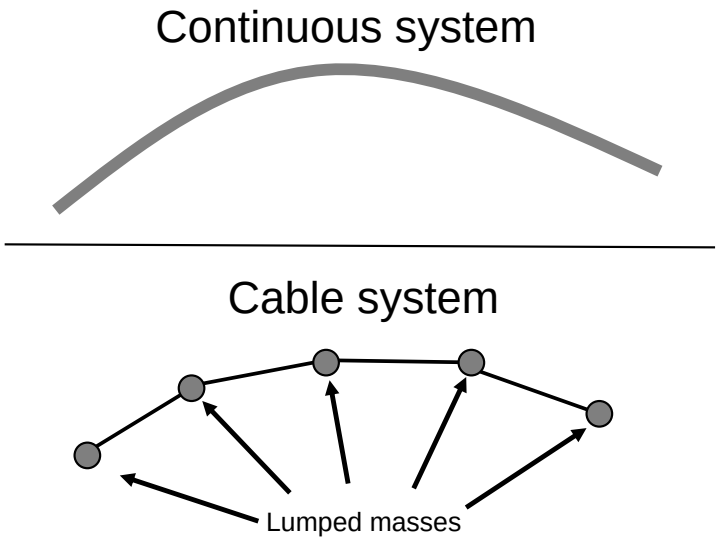

Figure 2.3: A picture to show the difference between the continuous distribution of mass in the beam model(top) as opposed to the lumped masses found in the cable model (bottom).

2.2.3 Coupled FSI Simulations

Another modeling approache is to fully couple the fluid and the solid by modeling both from first principles. For the case of a towed array, the governing equations are the incompressible Navier-Stokes equations to model the fluid, and the equations of elasticity to model the solid. The governing equations for a solid and a fluid are coupled through the use of appropriate boundary conditions on the interface.

A fully coupled fluid-structure interaction simulation from first principles is considered computationally expensive because it requires solving a non-linear coupled system of partial differential equations. The string approximation and the beam approximations resulted in solving a single linear differential equation, which is much less computationally demanding.

Research groups have performed full FSI simulations for cylinders in axial flow, but they have been clamped on both ends such as is found in nuclear fuel rods (Liu et al., 2012). There has also been a full FSI simulation of a clamped-free cylinder in axial flow by Fujita & Ohjuma (2010). However, these simulations have

a drastically different aspect ratio when compared to a towed array. To the best of the author's knowledge, a full FSI simulation for a towed array or cylinder with a similar aspect ratio has not been performed or published.

Recently several research groups have carried out full fluid-structure interaction simulations for axial flow. Z.G. Liu et al. (2012) of Hong Kong Polytechnic Institute have performed fully coupled simulations of cylinder clusters clamped at both ends under axial flow. This work was done to better model nuclear cooling rods. However, these simulations have a drastically different aspect ratio when compared to a towed array and do not have a free downstream end.

2.2.4 Recap by Decade

A cylinder in axial flow is an important fluid-structure interaction problem. The importance became apparent in the 1950's during the design of heat exchangers and cooling rods in nuclear power plants. The axial flow over nuclear cooling rods can cause them to vibrate. If the cooling rods are too closely spaced, they can collide and be damaged. Axial flow induced vibrations can also cause fatigue damage in materials. This is especially important for designing and predicting usable life for long service parts such as nuclear cooling rods.

In the 1960's two major papers were published. The first was Lighthill's paper on slender fish swimming, where he derives the inviscid forces on a fish. The other was Paidoussis' 1968 paper on the equation of motion for a flexible cylinder in axial flow and the experiments he conducted.

Paidoussis (1970) corrects an error in his 1968 paper. The error wasn't found during his experiments because it only has importance for long systems, such as a towed array. This was also the decade in which Ni & Hansen (1978) performed experiments for long slender cylinders in axial flow. Ni & Hansen's experiments had an aspect ratio of 500, which is much less than a towed array, but is one of the few experiments on large aspect ratio cylinders in axial flow.

In the 1980's, numerical simulations for towed arrays were becoming more common, such as in (Ablow, 1983; Chapman, 1984; Milinazzo et al., 1987; Traintafyllou, 1989). This is also the decade when the neutral point singularity of 1-D string model was overcome by A.P. Dowling (1988). Chapman (1984) performed simulations for the response of towed arrays during turns by using a string model that neglected

cable stretching and inertial forces.

Gagnon and Paidoussis (1994a; 1994b) published papers on the vibration of a cluster of cylinders in axial flow. These papers contain both theory and experimental validation. Further work was performed on the response of towed arrays during turns by Vaz & Patel (1995). Calkin (1999) developed a metamodel based off of curve fitting data to previous results from a large matrix of conditions. This metamodel was applied to simulations for the AN/SQR-18A towed array, and full scale sea trials were performed to validate his model. S.K. Srivastava & C. Ganapathy (1998) performed experiments in a wave basin on a towed array model to investigate the effects of loop maneuvers on the towed array.

Bhattacharyya (2000) used the finite element model for a towed flexible cylinder and used his model to examine the effect the shape of the downstream end has on stability. Gobat (2006; 2007) at the Woods Hole Oceanographic Institution performed numerical simulations with their CABLE program to build upon Chapman's work on the responses of towed array's during turns. Park's (2003) simulations of towed arrays did not directly simulate vortex shedding, but accounted for it by increasing the drag coefficients accordingly.

Recently several research groups have carried out full fluid-structure interaction simulations for axial flow. Z.G. Liu (2012) have performed fully coupled simulations of cylinder cluster clamped at both ends under axial flow. Their work was performed to improve models of nuclear cooling rods. There has also been full FSI simulations on a clamped-free cylinder in axial flow by Fujita & Ohjuma (2010). However, these simulations have a drastically different aspect ratio when compared to a towed array.

There is very little experimental data for cylinder with a length to diameter ratio comparable to that of a towed array. One example was performed by M. Obligado & M. Bourgoin (2013). The experiment was for a cable with an aspect ratio of 5×10^4 in a wind tunnel. In their experiments, spheres of different weights were attached to the end and the stability was examined. Their experiment for a cable without a sphere attached on the end was compared to the simulation results in (De Langre et al., 2007) and was found to agree.

2.3 State of the Art

The majority of simulations for towed cylinders fall into one of three categories. The first is to ignore bending stiffness and model the array as a 1-D string such as in (Dowling, 1988; Traintafyllou, 1989). The second category is a model which incorporates bending stiffness. This can be a simple model that treat the towed array as a uniform cylinder (Bhattacharyya et al., 2000) or more detailed one that incorporates aspects such as material non-linearities and non-uniform material properties along the length of the towed system (Grosenbaugh, 2007). However, none of these models take into account the effect the cylinder has on the flow of the fluid. Park (2003) does consider the effects of vortex shedding; however, the vortex shedding isn't directly simulated, and instead the drag coefficients are increased to account for presumed vortex shedding.

The third category is fully-coupled first-principles simulations. There are first principle simulations for a cylinder in axial flow, but to the author's knowledge there has not been a first principles simulation of a cylinder with a high aspect ratio in axial flow. As was previously stated, these types of simulations are computationally expensive in comparison to reduced order models.

2.3.1 Plan to Advance State of the Art

The author plans to advance the state of the art is to evaluate existing modelling techniques and select one or a combination of approaches that yield the best combination of physical realism and computational efficiency. To that end, a first principles simulation is compared to a published reduced-order model to determine situations where the reduced order model provides acceptable results. More specifically, this thesis is more interested in identifying areas where the reduced-order model fails to provide accurate results. Future work will then be performed to devise a reduced order model with a greater range of validity. Another goal of this thesis is to help make the decision on which model to use for a simulation by giving guidelines on how to balance accuracy and computational cost.

Chapter 3
First Principle solver

3.1 Introduction

Reduced-order models for towed arrays often assume that the flow field is constant; however, this is not the case because as the cylinder deforms it affects the fluid flow. This change in the fluid flow then affects the deformation of the cylinder, as seen in vortex induced vibrations (Paidoussis, 2004). Therefore a fully coupled fluid-structure interaction simulation is generally necessary to capture the effects of this two way coupling.

There are two approaches to coupling the governing equations for both the solid and the fluid. The first approach is to solve the equations for the fluid and solid simultaneously with one solver during each timestep. This approach is called monolithic and has been used in several codes such as Michler (2004) and Bazilevs (2008). The second approach is termed the partitioned approach. In the partitioned approach, separate solvers are used for the fluid and solid domains as was done in Campbell (2011), Matthies (2003), and Kittler (2006). Iterations are performed at each timestep until the solutions for both the solid and fluid converge to within some tolerance. The advantage to a partitioned approach is the ability to use solvers well-suited to the particular domain they are solving. The FSI solver used in this thesis uses a partitioned approach. To solve the fluid, the open source finite-volume solver OpenFOAM (Jasak, 1996) was used. The solid solver is an in-house finite element solver, FEANL (Campbell, 2011).

The primary difficulty in partitioned FSI is the efficient coupling of the disparate domains. This is due to the fact that the equations governing the solid are

often formulated from a Lagrangian frame while the fluid equations are often formulated using an Eulerian description. Communicating data between the two sets of governing equations is a non-trivial matter, and consequently, our governing equations are formulated using an Arbitrary Lagrangian-Eulerian method, or ALE method for short. The ALE method combines both the Lagrangian and Eulerian views by allowing grid points to move, but not forcing them to stay attached to a material point (Donea et al., 1982).

3.2 Governing equations

The governing equations for the fluid domain are the Navier-Stokes equations for an incompressible fluid. They are written in the ALE form to handle the mesh deformations (Masud, 1997), such that

$$\begin{cases} \rho \frac{\partial \mathbf{u}}{\partial t} + \rho(\mathbf{u} - \mathbf{u}^m) \cdot \bigtriangledown \mathbf{u} = - \bigtriangledown p + \mu \bigtriangledown^2 \mathbf{u} \\ \bigtriangledown \cdot \mathbf{u} = 0 \end{cases} \tag{3.1}$$

In the ALE N-S equations, ρ, p, t, μ, $\mathbf{u}$, and $\mathbf{u}^m$ represent fluid density, fluid pressure, time, fluid viscosity, fluid velocity, and mesh velocity respectively.

The cylinder is modeled as a hyperelastic solid by using Saint Venant-Kirchhoff model. This results in the solid exhibiting elastic behaviour for large deformations. The solid equation is formulated in the Lagrangian frame of reference as

$$\boldsymbol{S} = \lambda \mathrm{tr}(\boldsymbol{E}) \mathbb{I} + 2\mu \boldsymbol{E} \tag{3.2}$$

where $\boldsymbol{S}$ is the second Piola-Kirchhoff stress and $\boldsymbol{E}$ is the Lagrangian Green strain. λ and μ are the Lamé constants.

3.3 Solvers

The FSI solver uses a partitioned approach. The fluid is solved with the open source finite-volume solver OpenFOAM that uses the PISO algorithm (Issa, 1986) for an incompressible flow. The solid solver is an in-house finite element solver. A flow chart of the FSI solver is shown in Figure 3.1.

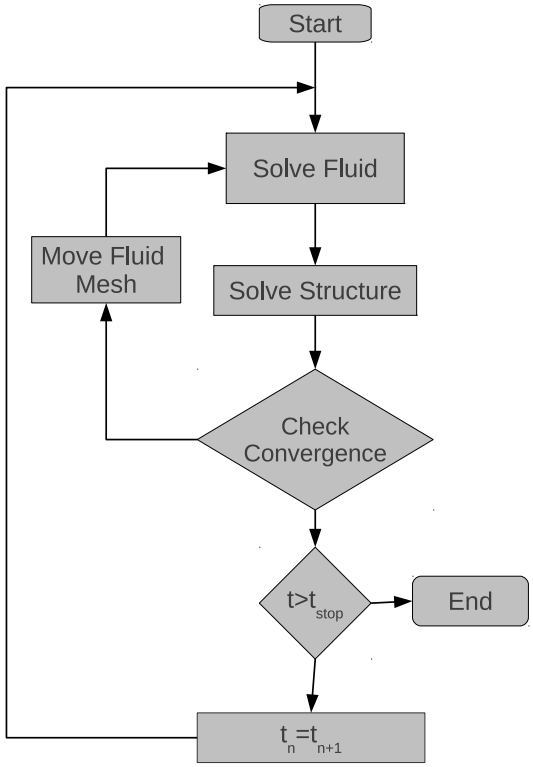

Figure 3.1: Flow chart for the FSI code.

3.3.1 Solid Solver - FEANL

The solid solver used was an in-house finite element code called FEANL (finite element analysis non-linear). FEANL has the capability to implement linear or quadratic continuous elements. Feanl is used as a black box solver in the algorithm.

3.3.2 Fluid Solver - OpenFOAM

The fluid solver used is the open-source finite volume solver OpenFOAM. The particular OpenFOAM solver for incompressible flows uses the PISO algorithm, which is an acronym for Pressure Implicit with Splitting of Operators. It is an iterative numerical scheme, and consist of alternating updates of the velocity field and the pressure field (Jasak, 1996).

The PISO algorithm is used to solve the incompressible Navier-Stokes equations, which consist of a continuity equation and a momentum equation. The non ALE

Navier Stokes equations are

$$\nabla \cdot \mathbf{u} = 0 \quad \text{(continuity)} \tag{3.3}$$

$$\frac{\partial \mathbf{u}}{\partial t} + \nabla \cdot (\mathbf{u} \otimes \mathbf{u}) - \nabla \cdot (\nu \nabla \mathbf{u}) = -\nabla p \quad \text{(momentum)} \tag{3.4}$$

The non-linearity in the convection term is solved iteratively with the following approximation

$$\nabla \cdot (\mathbf{u} \otimes \mathbf{u}) \approx \nabla \cdot (\mathbf{u^0} \otimes \mathbf{u^n}) \tag{3.5}$$

In this case $\mathbf{u^0}$ is the currently available solution and $\mathbf{u^n}$ is the new solution. The algorithm repeats until $\mathbf{u^0} \approx \mathbf{u^n}$ (Jasak, 1996). A flow chart illustrating the PISO algorithm is shown in Figure 3.2.

3.3.2.1 Derivation of pressure equation

A difficulty with solving the incompressible Navier-Stokes is the lack of a pressure equation. Issa (1986) derived a pressure equation using the momentum equations and the continuity equation. The semi-discretized momentum equation is

$$a_p U_p + \Sigma a_n u_n - \frac{u^0}{\Delta t} = -\nabla p. \tag{3.6}$$

A simplification is made by introducing

$$\mathbf{H}(\mathbf{u}) = -\Sigma a_n u_n + \frac{-u^0}{\Delta t}. \tag{3.7}$$

The result is

$$a_p \mathbf{u}_p = \mathbf{H}(\mathbf{u}) - \nabla p, \tag{3.8}$$

which after dividing by a_p is

$$\mathbf{u}_p = (\frac{1}{a_p})(\mathbf{H}(\mathbf{u}) - \nabla p). \tag{3.9}$$

Substituting this into the continuity equation, the pressure equation is obtained,

$$\nabla \cdot [(\frac{1}{a_p})(\mathbf{H}(\mathbf{u}) - \nabla p)] = 0, \tag{3.10}$$

which is rearranged to arrive at the elliptic equation for p,

$$\nabla \cdot [(\frac{1}{a_p})\nabla p] = \nabla \cdot [(\frac{1}{a_p})\mathbf{H}(\mathbf{u})]. \tag{3.11}$$

3.3.2.2 IcoFoam Algorithm

The PISO algorithm is used by the specific OpenFOAM solver called IcoFOAM. IcoFOAM uses the following algorithm to solve the fluid domain.

1. First set boundary conditions for the problem.

2. Next discretize and solve the momentum equation,

$$\frac{\partial \mathbf{u}}{\partial t} + \nabla \cdot (\mathbf{u}\phi) - \Delta(\nu \nabla \mathbf{u}) = -\nabla p, \tag{3.12}$$

   to compute an intermediate velocity field where the pressure from the previous time step is used, and ϕ is the flux of $\mathbf{u}$ from the last known value of $\mathbf{u}$.

3. Then store the discretization coefficients, a_p, from the last solution for velocity.

4. Store the velocity solution without the pressure gradient by using

$$\mathbf{u} = \frac{1}{a_p}\mathbf{H}(\mathbf{u}), \tag{3.13}$$

   and use this approximate velocity to calculate the interpolated face fluxes, ϕ.

5. Then calculate the new pressure,

$$\Delta(\frac{1}{a_p}p) = \nabla \cdot (\phi). \tag{3.14}$$

6. Correct the approximate velocity field by subtracting off the pressure gradient as a corrector

$$U- = \frac{1}{a_p}\nabla \cdot p, \tag{3.15}$$

   and update the boundary conditions.

7. If the solution is unconverged, return to step 3, otherwise move to the next time step.

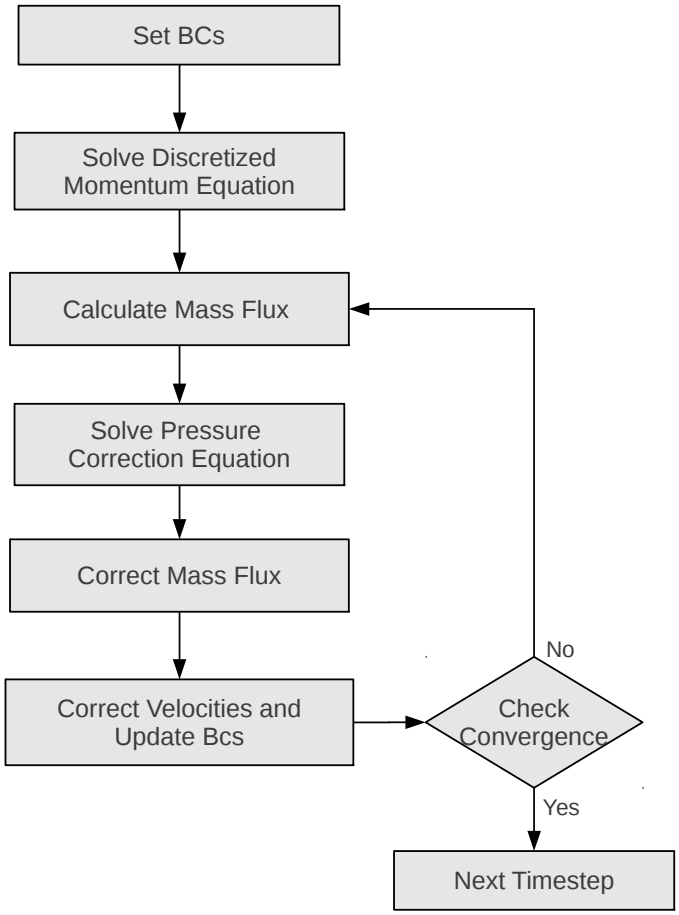

Figure 3.2: Flow chart for the PISO Algorithm.

3.4 Verification and Validation

The first principles solver has been verified and numerically validated by comparing to the Turek and Hron benchmark case shown in Figure 3.3 (Miller et al., 2014; Turek, 2006). The Turek-Hron benchmark case consists of a rigid and fixed cylinder in channel flow with a flexible trailing tail. The inlet velocity profile is parabolic and the cylinder is slightly off center to encourage the shedding of vortices. As vortices are shed from the cylinder they impinge on the flexible tail and excite it into vibration. A table of model properties is given in Table 3.1.

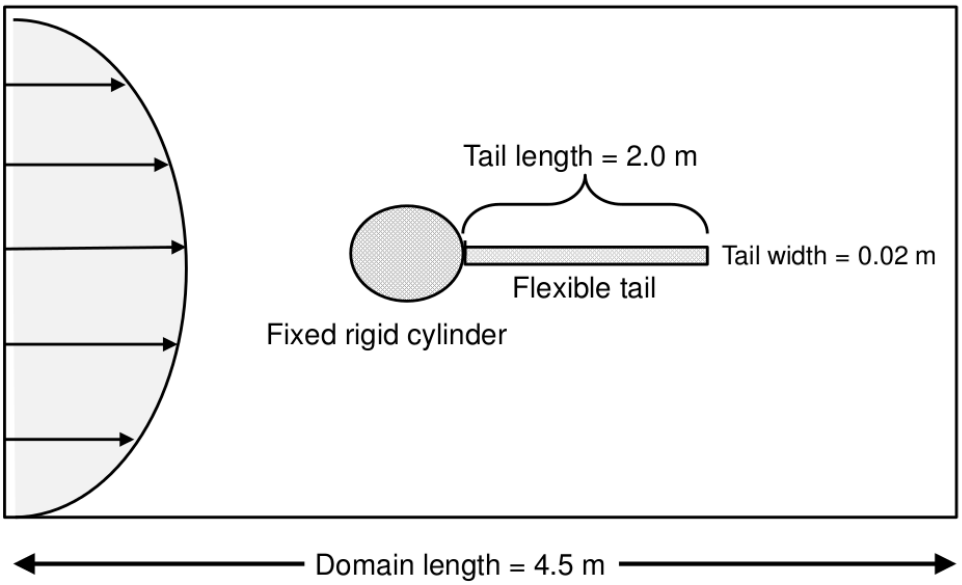

Figure 3.3: The setup for the long Turek case consists of channel flow with a parabolic inlet velocity. The cylinder is rigid and fixed in place. Attached to the cylinder is a flexible tail, and displacements are measured at the tip of the tail

Geometry parameters	Standard Turek case [m]	Long Turek case [m]
channel length	2.5	4.5
channel width	0.41	0.41
cylinder center position	(0.2,0.2)	(0.2,0.2)
cylinder radius	0.05	0.05
elastic structure length	0.35	2.0
elastic structure thickness	0.02	0.02

Table 3.1: Dimensions for the standard Turek case and for the long Turek case.

The first principles solver was used to simulate a Turek-Hron case but with a flexible tail with a higher aspect ratio of 100. The higher aspect ratio was achieved by increasing the length of the tail and the domain while keeping all other dimension the same. The tail length was increased from 0.35 meters to 2.0 meters while keeping the width the same as the standard Turek case. The overall domain length was increased from 2.5 meters to 4.5 meters. The height of the channel is 0.41 meters, which is the same as the standard Turek case. All boundary conditions

used in the long Turek case are the same as those found in the standard Turek case. This higher aspect ratio is closer to an actual towed array aspect ratio than the standard Turek case but still an order of magnitude smaller than an actual towed array.

As can be seen in Figure 3.4, the longer tail resulted in much smaller vibration amplitudes when compared to the original Turek-Hron benchmark. At first this seems counter intuitive and incorrect; however, this is in accordance with the Paidoussis model. The longer tail results in an increase in tension for the section of the tail closest to the cylinder. The increase in tension causes the section closest to the cylinder to become more rigid. The vortices shed by the cylinder first impinge on the flag where it is more rigid from tension. As the vortices move downstream, they dissipate and cause less lift on the flexible downstream tail section. The Paidousssis model would then apply to this flexible downstream section, and the Paidoussis model predicts that a cylinder in axial flow tends to be stable as long as the tail section is sufficiently blunt (Paidoussis, 2004).

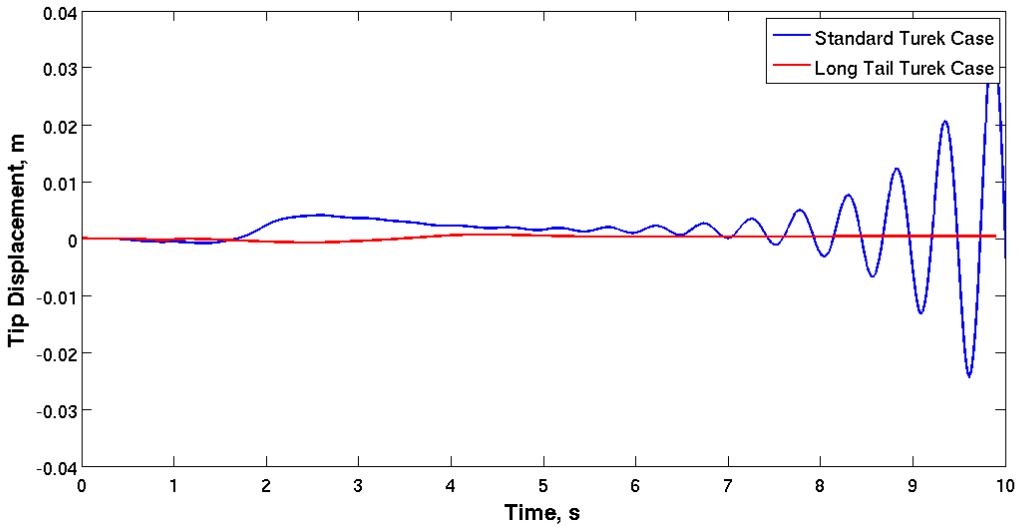

Figure 3.4: Vertical tip displacement versus time is plotted for the standard Turek case and the long-tail Turek case. It can be seen that there is very little displacement of the tip in the long tail case.

Chapter 4
Reduced-Order Model

4.1 Equation of Motion

The reduced-order model implemented in this thesis is the Paidoussis model for a cylinder in axial flow with uniform cross-sectional area (Paidoussis, 2004). A schematic of this is shown in Figure 4.1. It is a two dimensional model that gives the vertical displacement of the cylinder, y(x,t), as a function of position and time. The model was derived using a force balance argument; it is a combination of the inviscid forces derived in Lighthill's 1960 study on the swimming of fish and the viscous forces derived by Paidoussis. The model consists of a single linear partial differential equation:

$$EI\frac{\partial^4 y}{\partial x^4} + M(\frac{\partial}{\partial t} + U\frac{\partial}{\partial x})^2 y + \frac{1}{2}c_N\left(\frac{MU}{D}\right)\left(\frac{\partial y}{\partial t} + U\frac{\partial y}{\partial x}\right) - \frac{1}{2}MU^2\left[c_2 + c_T\frac{L-x}{D}\right]\frac{\partial^2 y}{\partial x^2} + m\frac{\partial^2 y}{\partial t^2} = 0 \quad (4.1)$$

- EI is the flexural rigidity.
- U is the speed of the fluid in the stream-wise direction.
- D is the diameter of the cylinder.
- L is the length of the cylinder.
- m is the mass per unit length of the cylinder.

- M is the mass of the displaced fluid.
- c_t and c_n are the longitudinal and normal drag coefficients, respectively. The ratio, c_n/c_t usually ranges between 0.5 for a rough cylinder and 1.5 for a smooth cylinder (De Langre et al., 2007).
- c_2 is the base drag coefficient which is typically between 0.1 and 0.7 (Paidoussis, 2004). A table of drag coefficients for various shapes can be found in chapter 10 of (Blevins, 1984).

Furthermore, each term is summarized as followed:

- $EI\frac{\partial^4 y}{\partial x^4}$ is from elementary beam theory
- $M(\frac{\partial}{\partial t}+U\frac{\partial}{\partial x})^2 y$ is the inviscid force
- $+\frac{1}{2}c_N(\frac{MU}{D})(\frac{\partial y}{\partial t}+U\frac{\partial y}{\partial x})$ is the normal viscous force
- $-\frac{1}{2}MU^2[c_2+c_T\frac{L-x}{D}]\frac{\partial^2 y}{\partial x^2}$ is the tangential viscous force
- $M\frac{\partial^2 y}{\partial t^2}$ is displaced fluid inertia from Newton's second law.

The boundary conditions for the downstream free end were previously derived by Paidoussis (Paidoussis, 1973). The first boundary condition, Equation (4.2), incorporates the forces acting on the tail and is dependent on the parameter f that is a measure of the slenderness of the tail section, and on l_2 which is the length of the end piece section. The value of f ranges from 0 to 1 where f=0 represents a completely blunt tail and a value of f=1 represents a perfectly streamlined tail. The second boundary condition required for the downstream free end is that there is no bending moment which is enforced by Equation (4.3).

$$\left(-EI\frac{\partial^3 y}{\partial x^3}-fMU(\frac{\partial y}{\partial t}+U\frac{\partial y}{\partial x})+(m+fM)l_2\frac{\partial^2 y}{\partial t^2}\right)_{x=L}=0 \tag{4.2}$$

$$\left(\frac{\partial^2 y}{\partial x^2}\right)_{x=L}=0 \tag{4.3}$$

As shown by Kheiri (2013), Equation (4.1) can be extended from two to three dimensions. In order to derive the model, certain assumptions had to be made. The first was that it is possible to simply add the inviscid force terms which had been derived earlier by Lighthill with the viscous pressure and friction force terms (Paidoussis, 1968; Lighthill, 1960). Paidoussis justifies the approximation of simply adding terms, by the reasoning that the viscous forces are not dominating the dynamics at high Reynolds number flows (Paidoussis, 1968). Other assumptions are:

- There is uniform cross-sectional area, A, mass per unit length m, and flexural rigidity EI.
- The angle of incidence θ and $\frac{\partial \theta}{\partial x}$ remain sufficiently small so that no separations occur in cross flow.
- Finally, the cylinder is located far enough away from the boundaries such that the boundaries have negligible effect on the cylinder's motion (Paidoussis, 1973).

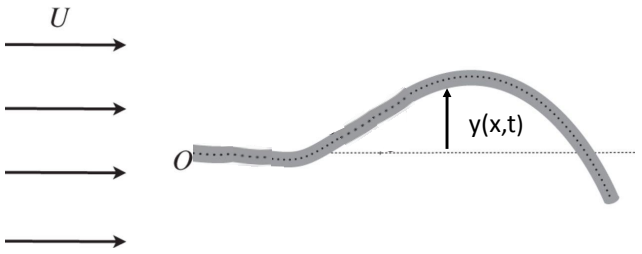

Figure 4.1: Physical diagram of the problem to be simulated (Singh et al., 2012). The displacement, y(x,t), from the centerline is the dependent variable.

4.2 Implementation

Rather than explore an analytical solution, a numerical approach to find an approximate solution is investigated. The finite element method was applied to the

Paidoussis equation using the open-source finite element library Deal.ii (Bangerth et al., 2013). Equation 4.1 can be written more compactly as

$$\alpha\frac{\partial^4 y}{\partial x^4}+\beta\frac{\partial^2 y}{\partial x^2}+\gamma\frac{\partial y}{\partial x}+\mu\frac{\partial^2 y}{\partial t\partial x}+\phi\frac{\partial^2 y}{\partial t^2}+\theta\frac{\partial y}{\partial t}=0, \tag{4.4}$$

where

$$\begin{aligned}
\alpha &= EI,\\
\beta &= MU^2-\frac{1}{2}MU^2(c_2+c_T\frac{L-x}{D}),\\
\gamma &= \frac{1}{2}c_N\frac{MU^2}{D},\\
\mu &= 2MU,\\
\phi &= 2M,\\
\theta &= \frac{c_N(MU)}{2D}.
\end{aligned}$$

By introducing $y'-w=0$, $w'-u=0$ and $\frac{\partial y}{\partial t}-v=0$, it is possible to write Equation 4.4 as a system of equations:

$$\begin{aligned}
y'-w &= 0\\
w'-u &= 0\\
v-\dot{y} &= 0\\
\alpha u''+\beta u+\gamma w+\phi\dot{v}+\theta v+\mu v' &= 0
\end{aligned} \tag{4.5}$$

Approximate solutions to Equations 4.5 are found by applying the Petrov-Galerkin method. Allow y,w,u,v $\in H^1(\Omega)$ where $H^1(\Omega)$ is the Hilbert space with first order weak derivatives in $L^2(\Omega)$, and Ω is the range of x. Also let φ be an arbitrary test function. Then by using the $L^2(\Omega)$ inner product which will be represented as $(\cdot,\cdot)$, Eqs. 4.5 can be written in weak form as

$$
\begin{aligned}
(\varphi, y')_\Omega - (\varphi, w)_\Omega &= 0 \\
(\varphi, w')_\Omega - (\varphi, u)_\Omega &= 0 \\
(\varphi, v)_\Omega - (\varphi, \dot{y})_\Omega &= 0 \\
(\varphi, \alpha u'')_\Omega + (\varphi, \beta u)_\Omega + (\varphi, \gamma w)_\Omega + (\varphi, \phi \dot{v})_\Omega + (\varphi, \theta v)_\Omega + (\varphi, \mu v')_\Omega &= 0.
\end{aligned} \tag{4.6}
$$

in which the equalities must hold for every φ. The system is transformed into a first order system in space by using integration by parts on the last equation to obtain

$$
\begin{aligned}
(\varphi, y')_\Omega - (\varphi, w)_\Omega &= 0 \\
(\varphi, w')_\Omega - (\varphi, u)_\Omega &= 0 \\
(\varphi, v)_\Omega - (\varphi, \dot{y})_\Omega &= 0 \\
-(\varphi', \alpha u')_\Omega + (\varphi, \beta u)_\Omega + (\varphi, \gamma w)_\Omega + (\varphi, \phi \dot{v})_\Omega & \\
+(\varphi, \theta v)_\Omega + (\varphi, \mu v')_\Omega + (\varphi, \alpha u')_{\partial\Omega} &= 0.
\end{aligned} \tag{4.7}
$$

4.2.1 Spatial Discretization

Currently, the problem is formulated in an infinite dimensional space, and must be discretized for the application of numerical techniques. For this reason, define the finite dimensional subspace, $\mathcal{V}_h(\Omega)$. Let y_h, w_h, u_h, $v_h \in \mathcal{V}_h(\Omega) \subset H^1(\Omega)$ and let φ_i be a basis for $\mathcal{V}_h(\Omega)$.

The trial solutions can be expressed as a linear combination of the basis functions:

$$
\begin{aligned}
y_h &= Y_j \varphi_j \\
w_h &= W_j \varphi_j \\
u_h &= U_j \varphi_j \\
v_h &= V_j \varphi_j,
\end{aligned}
$$

where Y_j,W_j,U_j, and V_j are the coordinates for the trial solution in the given basis.

The matrix form for numerical implementation is found to be:

$$\begin{bmatrix} 0 & 0 & 0 & 0 \\ 0 & 0 & 0 & 0 \\ A & 0 & 0 & 0 \\ 0 & 0 & 0 & C \end{bmatrix} \begin{bmatrix} \dot{Y} \\ \dot{W} \\ \dot{U} \\ \dot{V} \end{bmatrix} + \begin{bmatrix} B & -A & 0 & 0 \\ 0 & B & -A & 0 \\ 0 & 0 & 0 & -A \\ 0 & D & E & F \end{bmatrix} \begin{bmatrix} Y \\ W \\ U \\ V \end{bmatrix} = \begin{bmatrix} 0 \\ 0 \\ 0 \\ 0 \end{bmatrix}. \tag{4.8}$$

Here, the entries from the matrices have the following values:

$$A_{ij} = (\varphi_i, \varphi_j)$$

$$B_{ij} = (\varphi_i, \varphi_j')$$

$$C_{ij} = (\varphi_i, \phi\varphi_j)$$

$$D_{ij} = (\varphi_i, \gamma\varphi_j)$$

$$E_{ij} = -(\varphi_i', \alpha\varphi_j') + (\varphi_i, \beta\varphi_j) + (\varphi_i \mathbf{n}, \alpha\varphi_j')|_{x=0}^{x=L}$$

$$F_{ij} = (\varphi_i, \theta\varphi_j) + (\varphi_i, \mu\varphi_j').$$

4.2.2 Temporal Discretization

The theta-method scheme is chosen for time discretization. This method is a combination of the forward-Euler and the backward-Euler method. First, write Equation (4.8) in the more compact form,

$$M\dot{\xi} + K\xi = 0, \tag{4.9}$$

where M is the mass matrix, K is the stiffness matrix, and ξ is $[Y, W, U, V]^T$ The time derivative of ξ is approximated as

$$\dot{\xi} = \frac{\xi^{n+1} - \xi^n}{\Delta t} = \theta\xi^{n+1} + (1-\theta)\xi^n. \tag{4.10}$$

In Equation (4.10), θ is a parameter in the range of [0,1] where $\theta = 0$ corresponds to the foward-Euler method and $\theta = 1$ corresponds to the backward-Euler method. Substituting Equation (4.10) into Equation (4.9) yields

$$M\frac{\xi^{n+1} - \xi^n}{\Delta t} + K(\theta\xi^{n+1} + (1-\theta)\xi^n) = 0. \tag{4.11}$$

By multiplying both sides by Δt and grouping ξ^{k+1} terms together on one side,

$$(M + \Delta t\theta K)\xi^{n+1} = (M - \Delta t(1-\theta)K)\xi^{n} \tag{4.12}$$

is obtained. The initial condition, ξ^0, is known and can be used to solve for subsequent ξ^n by using the previous step, ξ^{n-1}.

4.3 Verification

4.3.1 Review of Method of Manufactured Solutions

The Method of Manufactured Solutions, or MMS, is a code verification technique used in numerical analysis. The word verification will refer to the mathematical exercise of making sure that the discrete equations are being solved correctly in the code. A short summary of the technique is presented. For a more detailed description please refer to Roache (1998).

The Method of Manufactured Solutions is a technique where an exact solution is chosen beforehand. This exact solution is then substituted back into the differential equation to obtain a forcing function. The original differential equation is now solved numerically with the forcing term included. Because the forcing term was derived to produce the already chosen exact solution, the exact solution is known. The advantage of knowing the exact solution is that it can be compared to the approximate solution arrived at by numerical methods to compute errors. Computed errors enables the ability to perform grid refinement studies to ensure the proper implementation of the numerical method.

It is worth noting that it is not necessary to choose a realistic exact solution. This is purely a mathematical exercise to ensure correct implementation of code. However, a more realistic exact solution might be helpful in convincing less mathematical experienced people or people unfamiliar with the technique of MMS.

4.3.2 Verification

The first step is to chose an exact solution. The exact solution used in this thesis is

$$y = \frac{1}{2}(1 - \cos(\pi t)) \sin(4\pi x) \tag{4.13}$$

$$w = 2\pi(1 - \cos(\pi t)) \cos(4\pi x) \tag{4.14}$$

$$u = -8\pi^2(1 - \cos(\pi t)) \sin(4\pi x) \tag{4.15}$$

$$v = \frac{1}{2}\pi \sin(\pi t) \sin(4\pi x). \tag{4.16}$$

The following values were chosen for the constants: U=1, M=1, D=0.01, L=1, c_2=0,and c_N=c_T=0.008.

Substituting Eqn. 4.13 into Eqn. 4.5 yields the residuals. These residuals are included as body forces i.e., right hand sides. The result is the following system of equations to be solved for verification:

$$\begin{aligned} y' - w &= 0 \\ w' - u &= 0 \\ v - \dot{y} &= 0 \\ \alpha u'' + \beta u + \gamma w + \phi \dot{v} + \theta v + \mu v' &= F_y, \end{aligned} \tag{4.17}$$

where F_y is the body force. F_y can be found by substituting the exact solution for y, w, u, and v into Equation (4.4). The result is

$$\begin{aligned} F_y =& 128\pi^4\alpha(1 - \cos(\pi t)) \sin(4\pi x) - 8\pi^2\beta(1 - \cos(\pi t)) \sin(4\pi x) \\ &+ 2\pi\gamma(1 - \cos(\pi t)) \cos(4\pi x) + \frac{1}{2}\pi^2\phi \cos(\pi t) \sin(4\pi x) \\ &+ \frac{1}{2}\pi\theta \sin(\pi t) \sin(4\pi x) + 2\pi^2\mu \sin(\pi t) \cos(4\pi x). \end{aligned}$$

Equation (4.17) can be written in discretized weak form as

$$\begin{bmatrix} 0 & 0 & 0 & 0 \\ 0 & 0 & 0 & 0 \\ A & 0 & 0 & 0 \\ 0 & 0 & 0 & C \end{bmatrix} \begin{bmatrix} \dot{Y} \\ \dot{W} \\ \dot{U} \\ \dot{V} \end{bmatrix} + \begin{bmatrix} B & -A & 0 & 0 \\ 0 & B & -A & 0 \\ 0 & 0 & 0 & -A \\ 0 & D & E & F \end{bmatrix} \begin{bmatrix} Y \\ W \\ U \\ V \end{bmatrix} = \begin{bmatrix} 0 \\ 0 \\ 0 \\ F_y \end{bmatrix}. \tag{4.18}$$

A,B,C,D,E, and F are the same as above and $Fy = (\varphi_i, F_y,)$ The boundary conditions and initial condition for the MMS solution are

$$y(0,t) = y(1,t) = 0 \tag{4.19}$$

$$u(0,t) = u(1,t) = 0 \tag{4.20}$$

$$v(0,t) = v(1,t) = 0 \tag{4.21}$$

$$y(x,0) = w(x,0) = u(x,0) = v(x,0) = 0. \tag{4.22}$$

The code was implemented in Deal.ii. The L_2 and L_∞ errors were computed after 2,000 time steps with a timestep of $dt = 0.001$. The number of time steps and step size was kept constant between the grid refinements. The implemented code yields the following convergence table for y, w, u, and v. A convergence rate of 2 is found for all variables as expected for Q1 elements. The results are shown in Tables 4.1, 4.2, 4.3, and 4.4. The error in the displacement are shown in Figure 4.2 and Figure 4.3 with the correct slop of 2.

Table 4.1: Refinement table for verification of y

cycle	# cells	# dofs	$\|y^* - y_h\|_{L_2}$		$\|y^* - y_h\|_{L_\infty}$	
0	32	132	1.849e-02	-	5.988e-02	-
1	64	260	4.603e-03	2.01	1.522e-02	1.98
2	128	516	1.149e-03	2.00	3.842e-03	1.99
3	256	1028	2.867e-04	2.00	9.593e-04	2.00
4	512	2052	7.120e-05	2.01	2.334e-04	2.04

Table 4.2: Refinement table for verification of w

cycle	# cells	# dofs	$\|w^* - w_h\|_{L_2}$		$\|w^* - w_h\|_{L_\infty}$	
0	16	68	6.597e-01	-	1.202e+00	-
1	32	132	1.652e-01	2.00	3.152e-01	1.93
2	64	260	4.135e-02	2.00	7.978e-02	1.98
3	128	516	1.034e-02	2.00	2.002e-02	1.99
4	256	1028	2.590e-03	2.00	5.025e-03	1.99

Table 4.3: Refinement table for verification of u

cycle	# cells	# dofs	$\|u^* - u_h\|_{L_2}$		$\|u^* - u_h\|_{L_\infty}$	
0	16	68	6.228e+00	-	1.082e+01	-
1	32	132	1.573e+00	1.98	2.878e+00	1.91
2	64	260	3.944e-01	2.00	7.305e-01	1.98
3	128	516	9.872e-02	2.00	1.834e-01	1.99
4	256	1028	2.474e-02	2.00	4.599e-02	2.00

Table 4.4: Refinement table for verification of v

cycle	# cells	# dofs	$\|v^* - v_h\|_{L_2}$		$\|v^* - v_h\|_{L_\infty}$	
0	16	68	6.433e-02	-	1.306e-01	-
1	32	132	1.570e-02	2.04	3.200e-02	2.03
2	64	260	3.901e-03	2.01	7.983e-03	2.00
3	128	516	9.767e-04	2.00	2.003e-03	1.99
4	256	1028	2.608e-04	1.90	5.875e-04	1.77

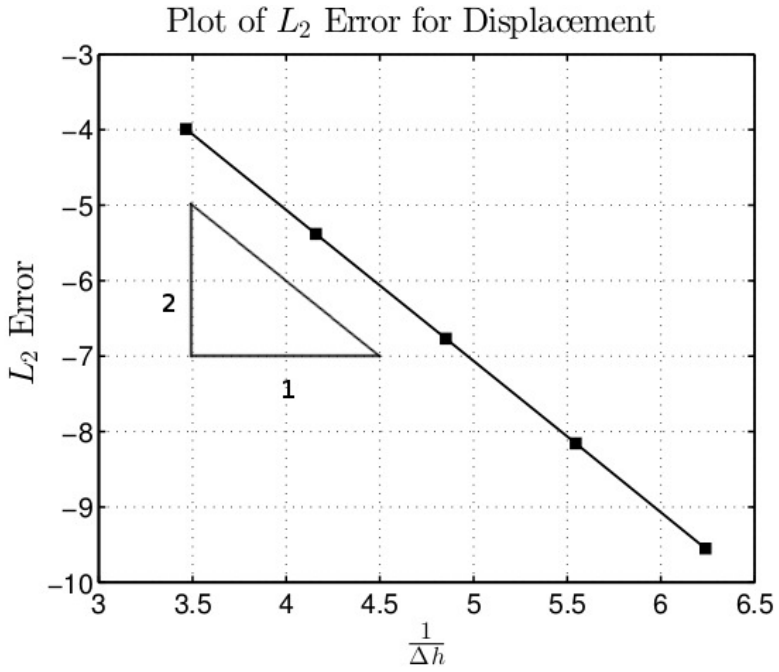

Figure 4.2: Log-log plot of L_2 error for displacement for grid refinement study. Error was calculated after 2,000 timesteps with a step size of 0.001

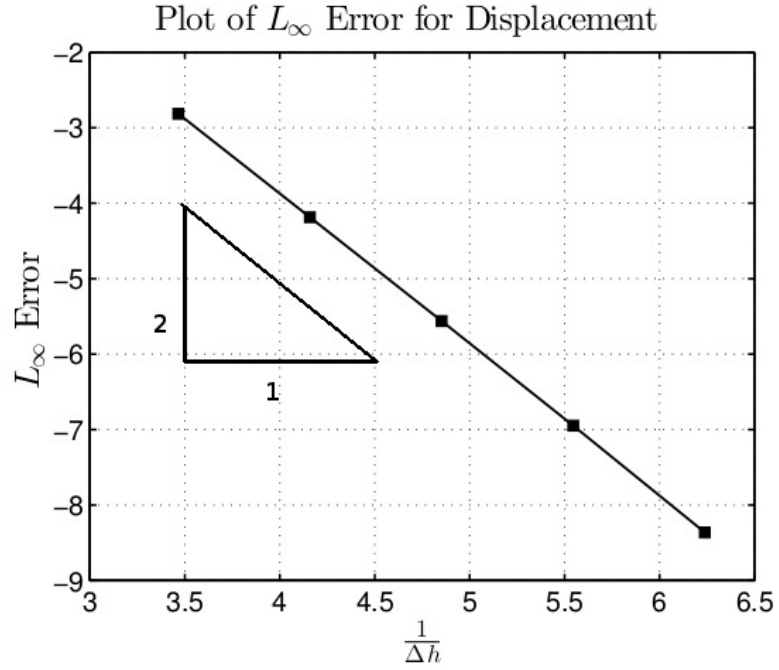

Figure 4.3: Log-log plot of L_∞ error for displacement for grid refinement study. Error was calculated after 2,000 timesteps with a step size of 0.001

4.4 Best Practices

It is important to ensure that a dynamic simulation conserves energy. A simple test case was used to verify that the energy in the system is being conserved. The test case had $\beta = 1$, $\phi = -1$, and all other coefficients 0. This corresponds to the wave equation in 1-D. The total energy of the system is equal to the kinetic energy plus the potential energy from stretching the string.

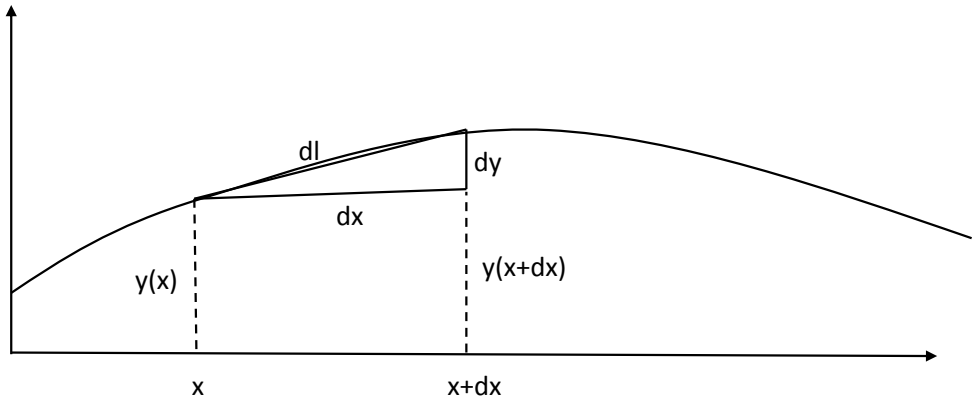

Figure 4.4: Close-up of a vibrating string used in the derivation of the energy of the system

The formula for the kinetic energy is

$$\text{Kinetic Energy} = \int_0^L \frac{1}{2} m v^2 \text{dx}, \tag{4.23}$$

where m is the mass per unit length. For this simulation $m = 1$.

The potential energy comes only from the stretching of the string as seen in Figure 4.4. The change of length of the string over an arbitrary small interval dx is required. The length of the string over the interval [x, x+dx] is dl. Assuming small deformations, Pythagorean's theorem can be used to write dl as

$$\text{dl} = \sqrt{\text{dx}^2 + \text{dy}^2} = \text{dx}\sqrt{1 + \left(\frac{\text{dy}}{\text{dx}}\right)^2}. \tag{4.24}$$

For small deformations, the square root can be approximated as

$$\mathrm{dx}\sqrt{1+\left(\frac{\mathrm{dy}}{\mathrm{dx}}\right)^2} \approx \mathrm{dx}\left(1+\frac{1}{2}\left(\frac{\mathrm{dy}}{\mathrm{dx}}\right)^2\right). \tag{4.25}$$

The change in length is then

$$\text{stretch} = \text{new length} - \text{old length} = \mathrm{dl} - \mathrm{dx} = \frac{1}{2}\left(\frac{\mathrm{dy}}{\mathrm{dx}}\right)^2 \mathrm{dx}. \tag{4.26}$$

Energy is force times distance. By assuming constant tension in the string, the potential energy is then stretch multiplied by tension. For this case, the tension was chosen to be 1. By integrating over the whole length of the string, and substituting in $w = \frac{\mathrm{dy}}{\mathrm{dx}}$ the total potential energy can be computed as

$$\text{Potential Energy} = \int_0^L \frac{1}{2} w^2 \mathrm{dx}. \tag{4.27}$$

By adding the kinetic energy to the potential energy, the total energy of the system is

$$\text{Total Energy} = \text{K.E.} + \text{P.E} = \int_0^L \frac{1}{2} m v^2 \mathrm{dx} + \int_0^L \frac{1}{2} w^2 \mathrm{dx}. \tag{4.28}$$

The total energy of the system was graphed as a function of time for two different time stepping methods. The first was for $\theta = 1$, which corresponds to the implicit backward-Euler time-stepping scheme. The results are shown in Figure 4.5. It can be seen from Figure 4.5 that the total energy of the system decays. This is to be expected for an implicit time-stepping scheme.

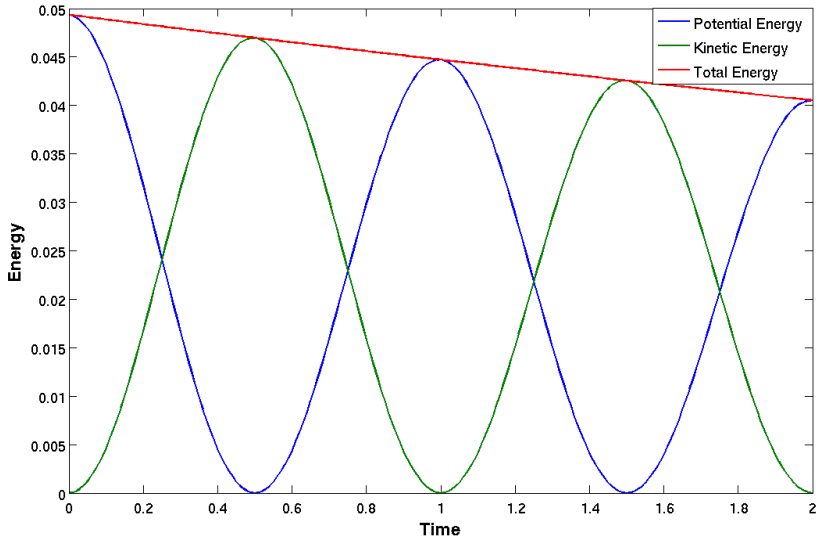

Figure 4.5: Energy of the system solved using Backward-Euler time-stepping, $\theta = 1$

Next the simulation was performed with $\theta = 0.5$. The kinetic energy, potential energy, and total energy were again calculated. As can be seen in Figure 4.6 the energy for $\theta = 0.5$ is conserved.

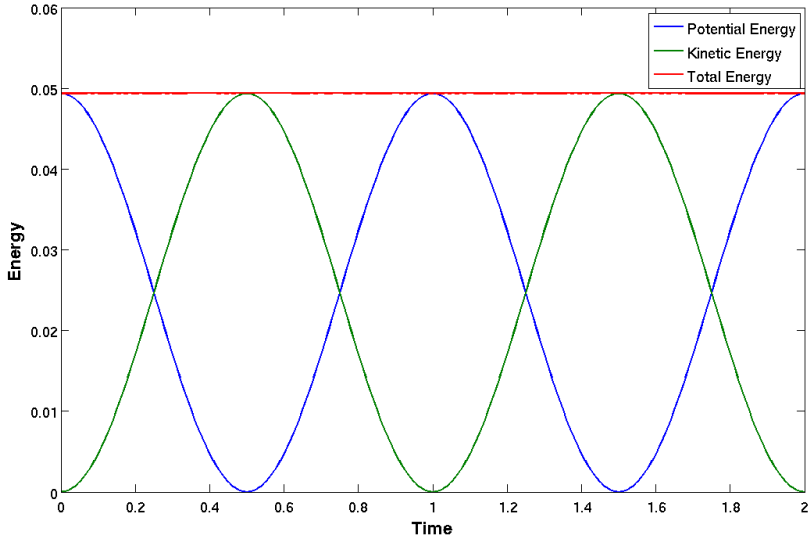

Figure 4.6: Energy of the system solved using Crank-Nicholson time-stepping, $\theta = 0.5$

Chapter 5
Model Comparison

5.1 Introduction

In this chapter, results for the Paidoussis model are compared to results from a full-order model. As explained previously, the reduced order model should be used to predict stability of set-ups and not specific displacements of the cylinder. If an instability is formed, the full order model, unlike the reduced-order model, will be able to predict the existence and amplitude of limit cycles.

5.2 Comparison case

The work of Paidoussis (2002) is followed and in an attempt to recreate his experimental results computationally. Therefore, the following parameters are used for a cylinder in water.

- $D = 1.676 \times 10^{-2}\,m$
- $L = 0.330\,m$
- $EI = 7.68 \times 10^{-3}\,Nm^2$ or $E = 1.98 \times 10^{6}\,N/m^2$
- $m = 0.25\,kg/m = 1{,}141\,kg/m^3$
- $U \in 1,2,4,6\ m/s$

During these experiments it was recorded by Paidoussis that the dynamics of the cylinder were most sensitive to changes in flow velocity. For this reason, flow

velocity is the parameter varied. The range for velocity will be between zero and six meters/second, which is the range that Paidoussis performed his experiments. It has been decided to simulate the cylinder with two different tail pieces. The first is a cylinder with a blunt downstream end, and the second is a well streamlined downstream end. These two cases were run at various fluid velocities and the behaviour of both models are compared in subsequent sections.

For the reduced order model the cylinder must be given an initial displacement or velocity, otherwise the Paidoussis model would return the trivial solution of zero displacement and zero velocity for all time. This is not the case for the first principles model which can have initial conditions of zero displacement and zero velocity.

5.2.1 Reduced-Order Model Setup

The reduced order model had an initial displacement of $y = x^4/24 - x^3L/6 + x^2L^2/4$. This initial displacement was chosen because it satisfies the boundary conditions of $y = 0$ and $y' = 0$ on the clamped end, x=0, as well as the moment free condition of $y'' = 0$ on the free downstream end, x=L. The simulations were run for 1000 timesteps at a timestep of 0.01 seconds. A simulation could usually be completed in about ten minutes.

As previously stated, since a linear model is being used, the displacement of the cylinder either converges to zero or diverges to infinite displacement. A convergence to zero represents a stable solution. Divergence is characterized by the tip displacement heading monotonically towards infinity in the reduced order model. Flutter is characterized by a flapping of the tip displacement. Because flutter is an instability, the amplitude of the oscillations grow exponentially towards infinity.

5.2.2 First Principles Simulation Setup

The full order model had a uniform inlet velocity coming from the left in Figure 5.2. The cylinder is clamped on the upstream end and free on the downstream end. The initial condition for the cylinder is zero displacement and zero velocity. The top and bottom boundaries have slip boundary conditions. The pressure is set to zero for the outlet and the gradient is set to zero for the inlet and for the cylinder-fluid interface. A two-dimensional case was run because the Paidoussis

model is a two-dimensional model.

The mesh for the full order model consisted of approximately 18,000 hexahedron cells. Mesh studies were not performed for the full order model. However, Paidoussis' reported experimental data on the instabilities observed for the simulation cases performed (Paidoussis, 2004). Paidoussis also reported a cylinder tip-displacement of around one to two cylinder diameter lengths (Paidoussis, 2004) for the instabilities. An example of a divergence and flutter instabiltiy from Paidoussis experiments can be seen in Figure 5.1. Since the full order simulations were within the range observed in Paidoussis' experiments, it was determined that the meshes were sufficient.

The Reynolds number for the slowest case is 330,000 if the length of the cylinder is used for the characteristic length. This means the simulations are turbulent. However, a turbulence model was not used in the full order simulations. It was determined to be unnecessary to utilize a turbulence model because the full order simulations without a turbulence model had instabilities and amplitudes that were both in agreement with Paidoussis' experiments. A turbulence model would have been necessary if the precise value of the instability amplitude was of interest. But the reduced order model does not predict instability amplitude. Thus, a precise value for the instability amplitude is not required to make a comparison between the two models. For this reason, no turbulence model was used during the full order simulations.

The time it took for a full order simulation to run was dependent on the velocity. Higher velocity simulations required a smaller timestep to keep the Courant number down, and thus resulted in a longer runtime. All simulations were run on a single computer using a quad CPU with 2.83 GHz processor. It took roughly 4 days for a simulation at a velocity of 1 m/s to run. It took about 2 weeks to run a simulation with a velocity of 6 m/s.

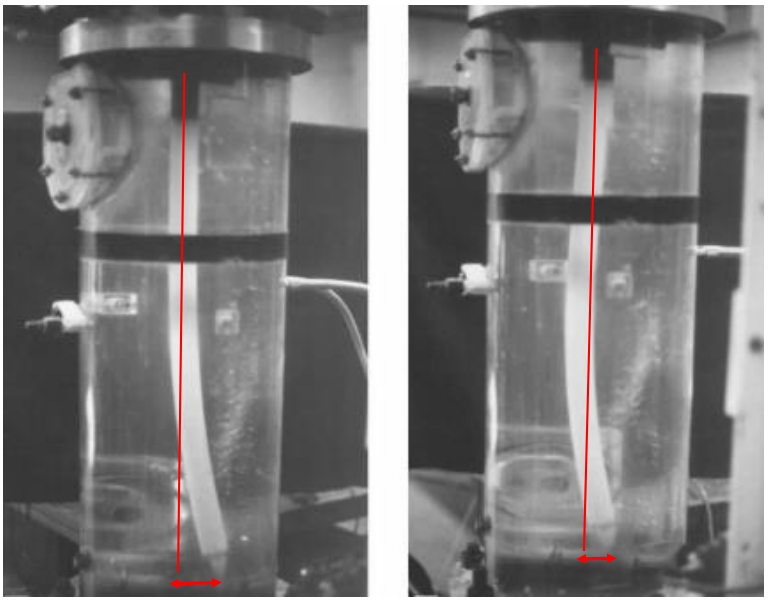

Figure 5.1: Pictures from Paidoussis' experiments for a cylinder in axial flow. The picture on the left shows a divergence instability and the picture on the right shows a flutter instability. The center line was drawn in to emphasize the displacement of the cylinder from a neutral position. Both figures show instability amplitudes between one and two cylinder diameters. The instability amplitude of the full order model falls within this range.

5.3 Clamped-free with a blunt end comparison

Full order simulations were performed for a cylinder in axial flow with an unconstrained blunt downstream end. The setup for the simulation is in Figure 5.2. The reduced order model predicts that this case is stable for all flow speeds tested. For all speeds simulated, the full order model had a maximum tip displacement of less than 1 mm. The displacement for an inlet velocity of four meters per second is shown in Figure 5.4. It is then reasonable to call the cylinder stable which is in agreement with the reduced order model prediction. Although the same solution was arrived at for both models, the reduced order model was able to make these prediction in a matter of minutes as opposed to the full order model that required days to run. The grid used for the full order model can bee seen in Figure 5.3.

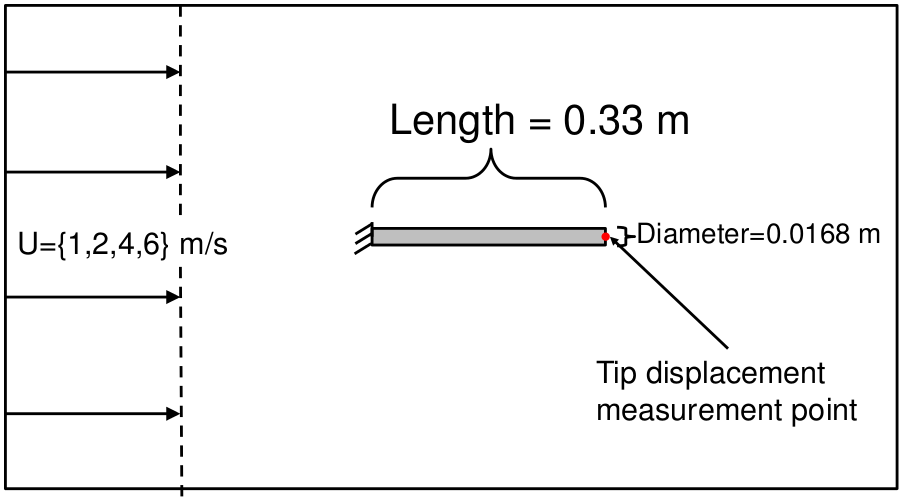

Figure 5.2: Simulation set-up for the the full order model with a blunt downstream end. The cylinder is clamped on the upstream end and the downstream end is free. There is also uniform inlet velocity and slip boundary conditions on top and bottom of the channel.

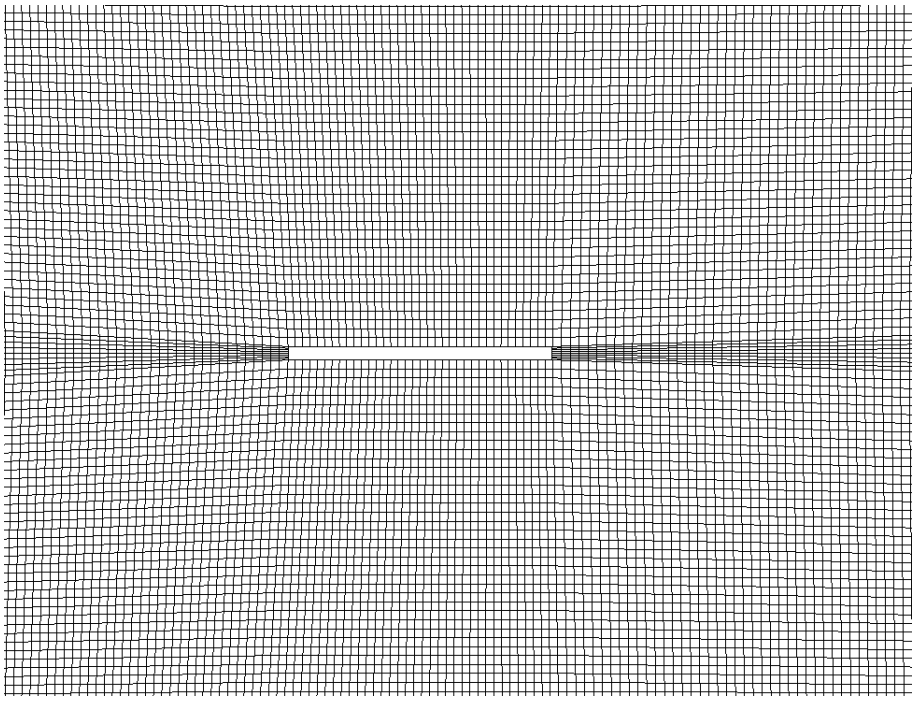

Figure 5.3: The grid used for the first principle simulations with a blunt tail consisted of approximately 18,000 hexahedron cells.

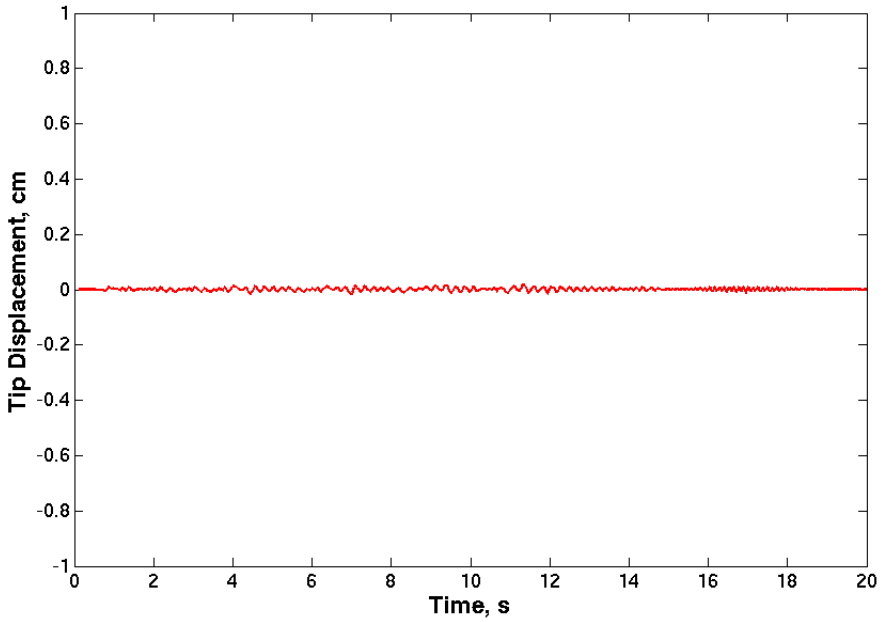

Figure 5.4: Displacement vs time for a blunt end and U= 4 m/s. Similar results were obtained for other cases as well.

5.4 Clamped-free with a streamlined end comparison

Simulations were also run for a cylinder with a more streamlined tail. A picture of the cylinder shape used in the full order model simulation can be seen in Figure 5.5. The number of cells in the full order model simulation is the same as used in the blunt tail simulations. The f-value in the Paidoussis model is a measure of how streamlined the tail section is and ranges from 0 to 1 where f=0 represents a perfectly blunt tail and f=1 represents a perfectly streamlined tail. There is not a precise way of calculating the value of f for a given tail piece. Thus, to directly compare the two models, it must be done qualitatively. Basic trends can still be compared. The f-value affects the critical velocities that divergence and flutter begin. It's noted that the reduced order model used returned the same stability predictions for f values of f=0.6-0.9 for the comparison cases ran. It is reasonable to assume the true f value falls into this range because the tailpiece is fairly well streamlined. The grid used by the full order model is shown in Figure 5.6.

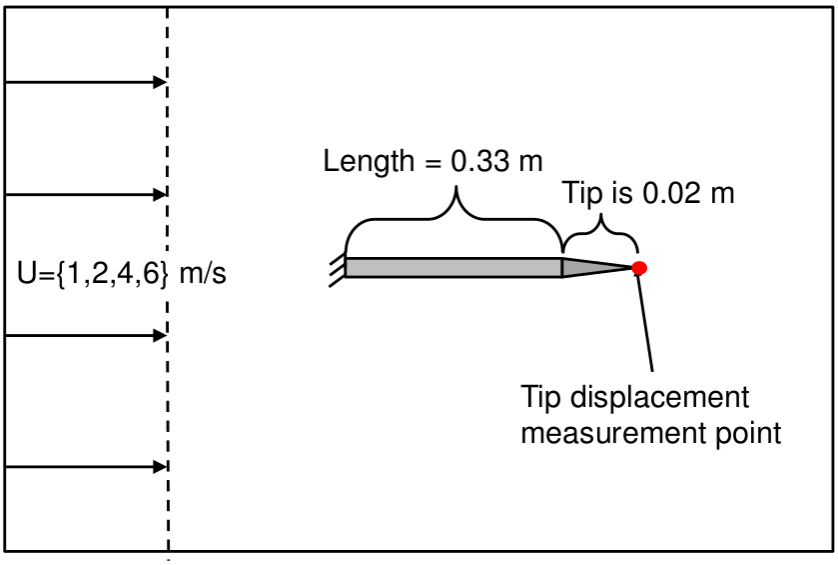

Figure 5.5: Simulation set-up for the the full order model with a streamlined downstream end. The cylinder is clamped on the upstream end and the downstream end is free. There is also uniform inlet velocity.

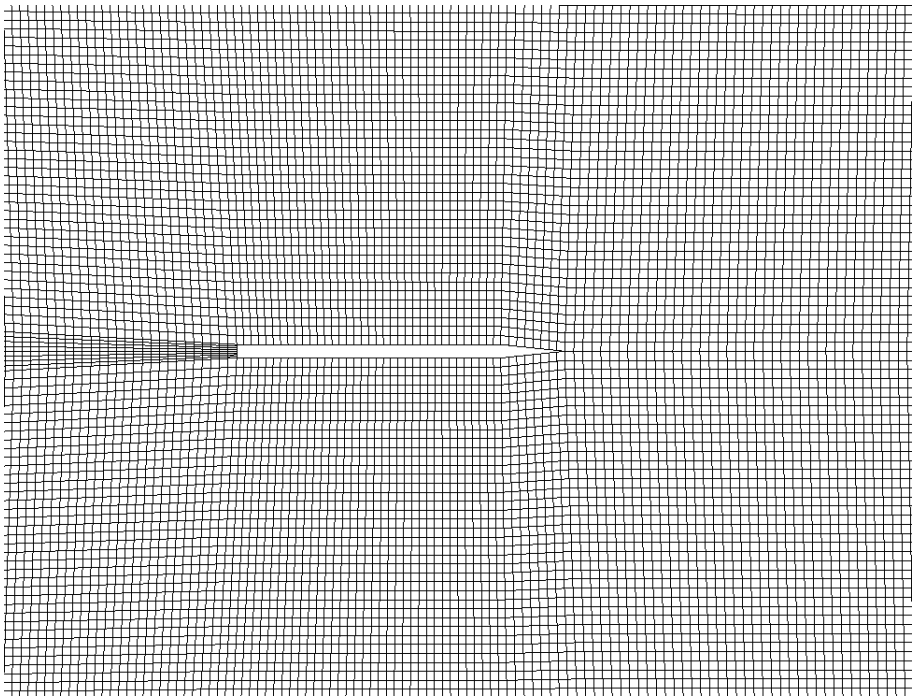

Figure 5.6: The grid used for the first principle simulations with a streamlined tail consisted of approximately 18,000 hexahedron cells.

5.4.1 U=1

The maximum displacement experienced by the tip in the full order simulation was approximately 1 mm after 20 seconds. The reduced order model predicts a stable configuration. Although the full order model simulation resulted in the cylinder experiencing some displacement(see Figure 5.5), it still shows the same conclusion as the reduced order model.

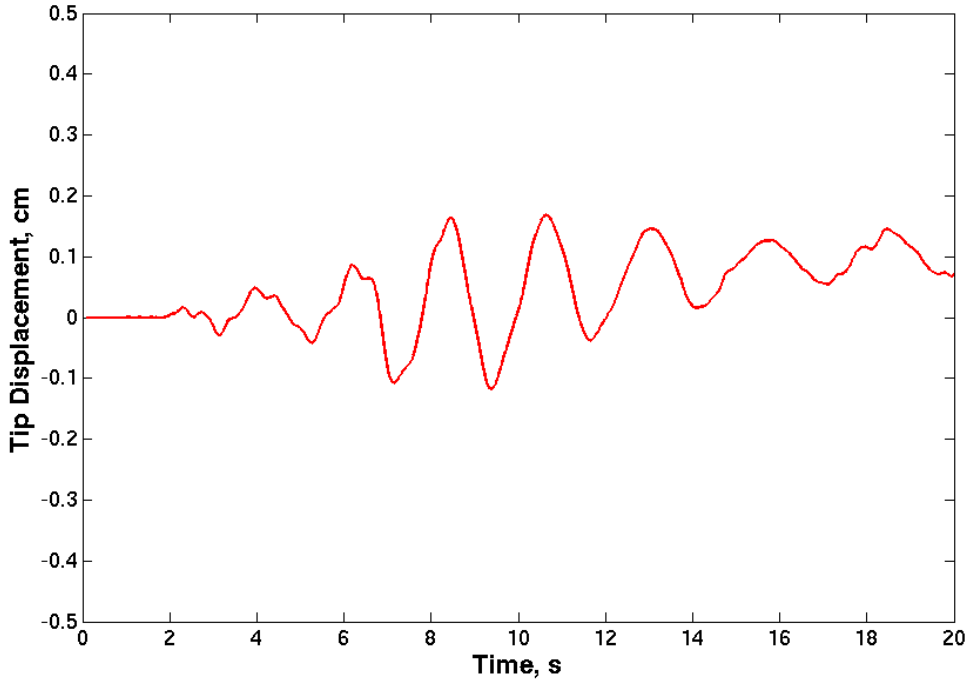

Figure 5.7: Tip displacement (cm) from the full order model for a streamlined tail setup vs time (s) with U=1 m/s. The figure shows that the configuration can be considered stable since the max displacement was roughly only a millimeter after 20 seconds.

5.4.2 U=2

As can be seen in Figure 5.8 and Figure 5.9, the full order model simulation is beginning to show signs of divergence when using an inlet speed of 2 m/s. In the full order simulation the tip displaces a distance of 1.5 cm and then holds there. The divergence is caused by lift being generated by the streamlined tail piece. The results in a force displacing the tip. This is in agreement with the reduced order

model which predicts divergence for any f-value between 0.5 and 0.9 with this configuration. It is worth noting again that the reduced order model is unable to predict that the cylinder diverges with an amplitude of 1.5 cm, however it did correctly predict that a divergence instability would form. Also Paidoussis does not report amplitude of displacement for his experiments but he does mention for his experiments there was displacement between 1 to 2 times the cylinder diameter (Paidoussis, 2004). The simulations had a displacement of around 1.5 centimeters which is in agreement with the experimental results of a one to two cylinder diameter displacement. Furthermore, qualitatively the shape is similar to the divergence experimental result shown in Figure 5.1. This gives us confidence that our full order simulation is accurate.

Notice that although the simulation was set-up to be symmetrical, round-off error could be the cause for the cylinder to diverge to a specific side. There are numerous places where round off could have occurred in the full order model. One possibility is in the mesh creation. The node coordinates for the mesh are floating point values which are susceptible to round off error. There could also be round off error occurring in the solvers. Round-off error could be the cause for the cylinder to initially choose a side to diverge to.

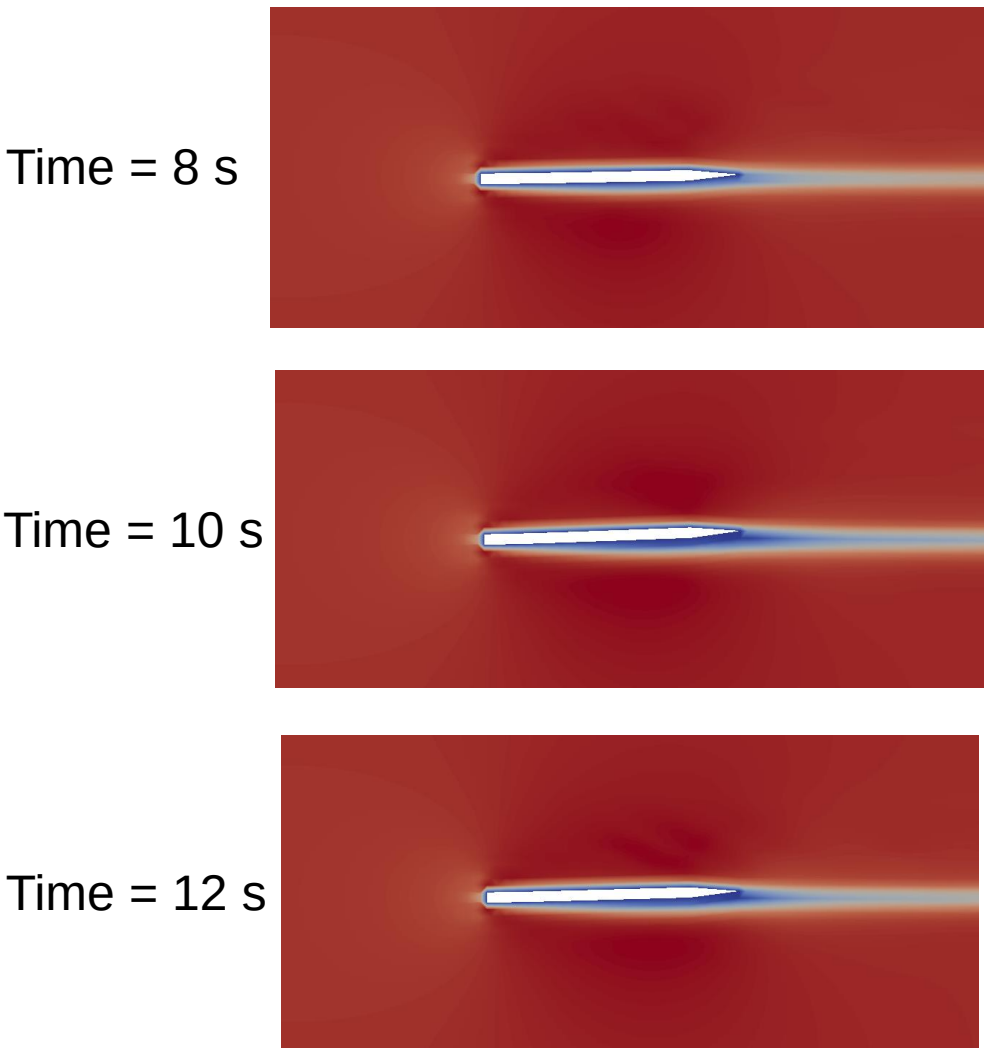

Figure 5.8: Results from the full order simulation with a streamlined tail at various times with U=2 m/s shows the cylinder has a divergence instability.

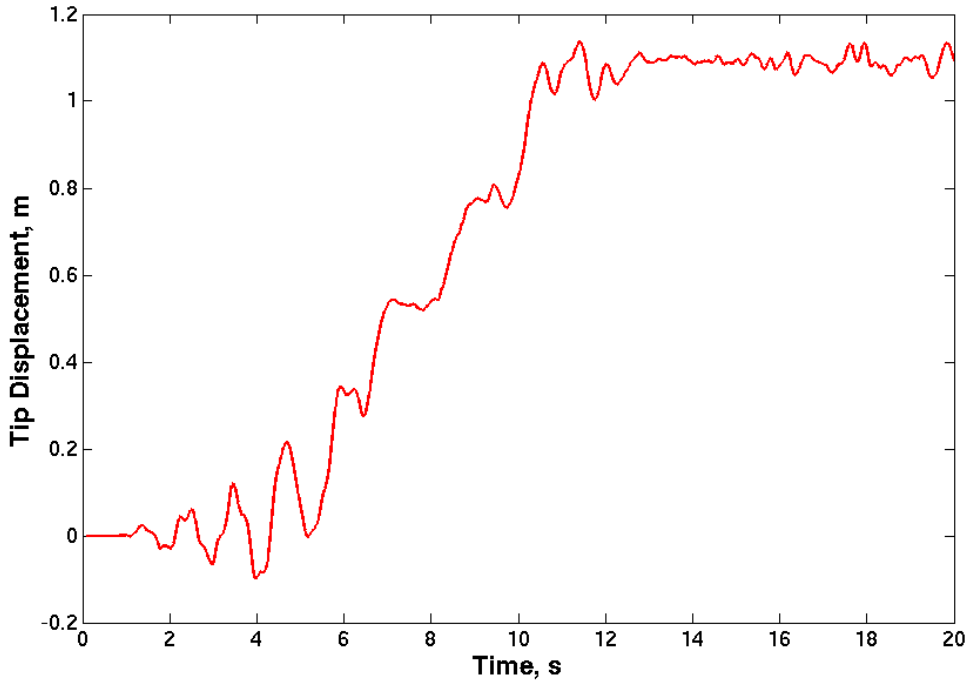

Figure 5.9: Tip displacement (cm) from the full order model for a streamlined tail setup vs time (s) with U=2 m/s. The figure shows the tip displacement having an average displacement of roughly 1.5 cm which clearly show a divergence instability.

5.4.3 U=4

The full order model simulation using U=4 m/s still shows divergence as the dominating instability with an average displacement of about 1.2 cm. The shape of the cylinder can be seen in Figure 5.10. Tip displacement vs time is shown in Figure 5.11. Again, the divergenec is a result of the lift generated by the end piece. Oscillations around the divergence amplitude are greater for U=4 m/s than for U=2 m/s. The oscillations are still small at roughly 0.5 mm, but they show the system is beginning to form a flutter instability. Figure 5.12 shows that the reduced order model predicts that only a divergence instability should form at this speed. Since divergence is still the dominating instability, it is reasonable to say that the full order model and reduced order model are still in agreement in the instability prediction. The divergence amplitude is also still in agreement with Paidoussis' experimental results (Paidoussis, 2004). Again, the choice of instability direction can be attributed to round-off error.

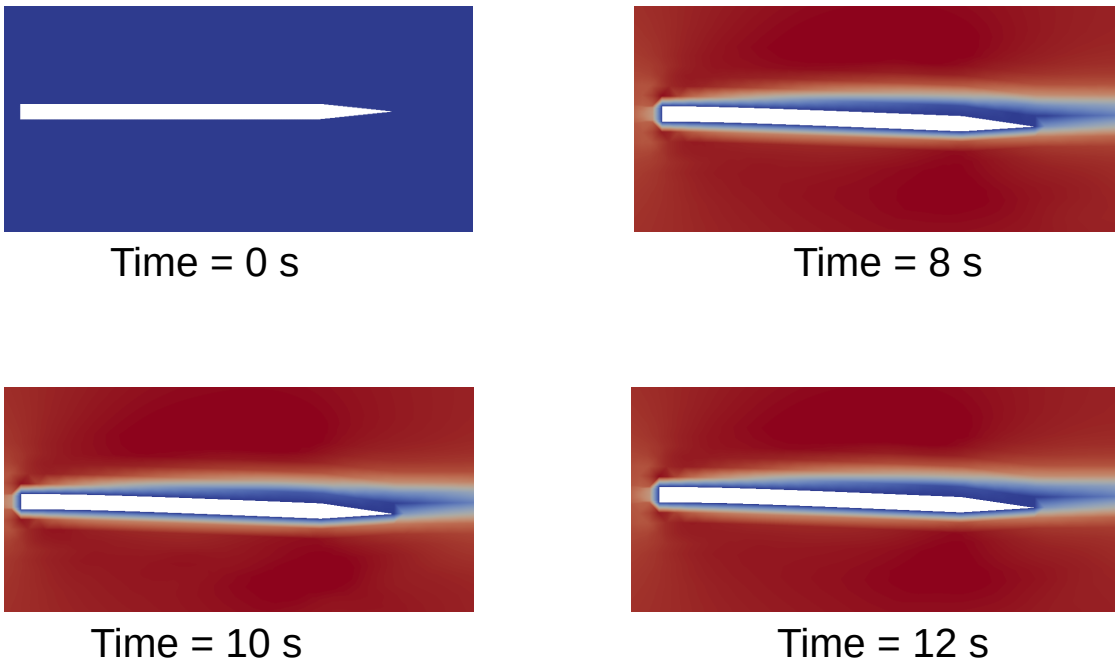

Figure 5.10: Results from the full order simulation with a streamlined tail at various times with U=4 m/s shows the cylinder forms a divergence instability. This is similar to the response when U=2 m/s.

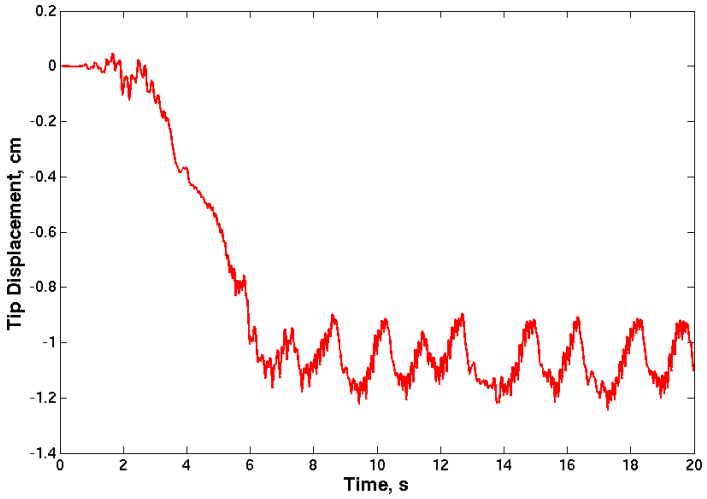

Figure 5.11: Tip displacement (cm) from the full order model for a streamlined tail setup vs time (s) with U=4 m/s. The figure shows the tip displacement has a divergence instability but oscillations are starting to grow. This shows that flutter is beginning to form.

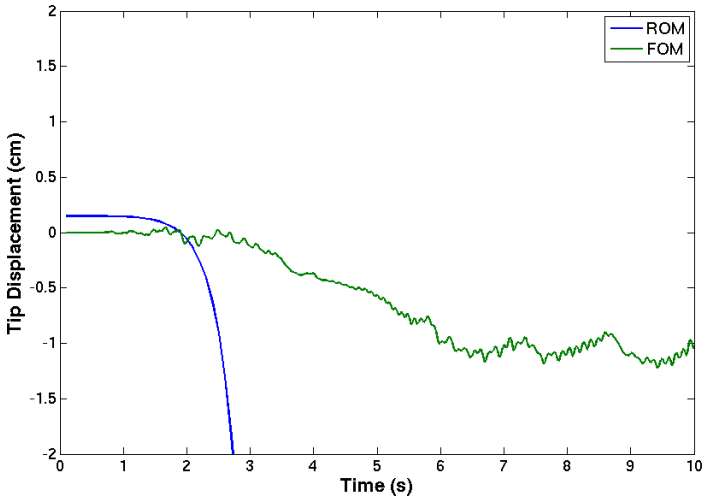

Figure 5.12: Tip displacement (cm) from both the full order model and the reduced order model for a streamlined tail setup vs time (s) with U=4 m/s. The reduced order model shows the cylinder will diverge by monotonically converging to negative infinity

5.4.4 U=6

For U=6 m/s, second mode flutter has become the dominating instability in the full order model. The cylinder shape for various times is shown in Figure 5.13. Figure 5.14 shows the tip displacement as a function of time. Figure 5.16 shows that the flutter is not centered around zero. This provides evidence that the cylinder is also unstable in the divergence mode as well. The reduced order model predicts flutter at the speed of U=6 m/s. Of course, as has been previously been pointed out, the full order model is able to predict the amplitude of each instability.

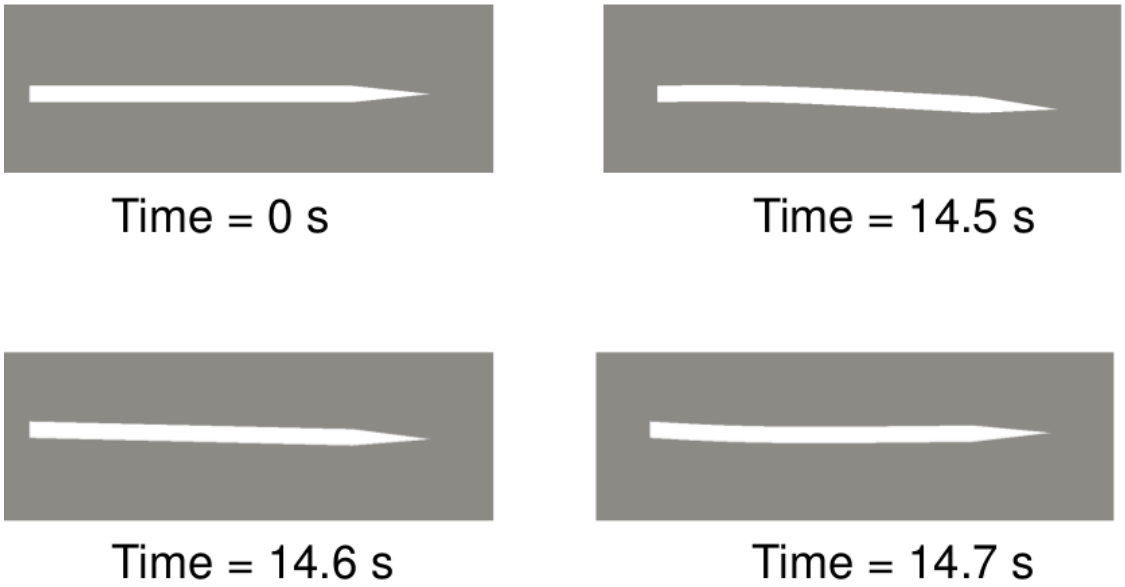

Figure 5.13: Results from the full order simulation with a streamlined tail at various times with U=6 m/s shows the cylinder has a flutter instability.

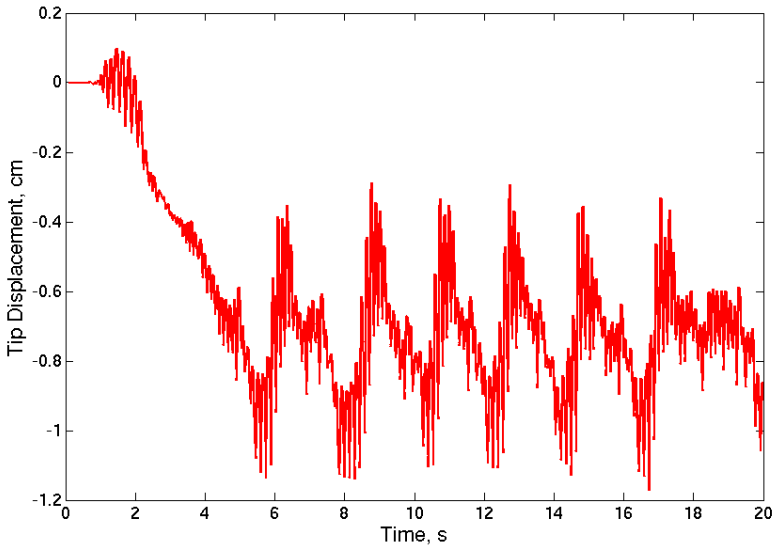

Figure 5.14: Tip displacement (cm) from the full order model for a streamlined tail setup vs time (s) with U=6 m/s. The figure shows a divergence instability forms first but flutter oscillations are starting to grow. The oscillations appear to be centered around the divergence average displacement of 0.8 cm.

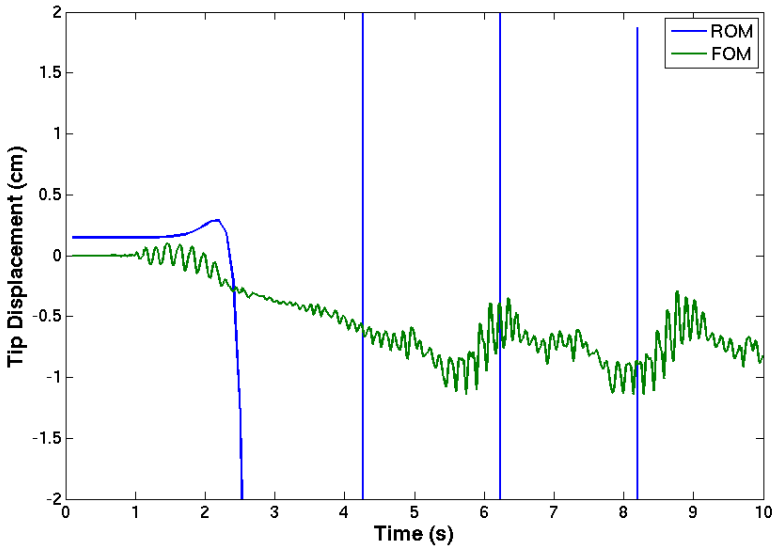

Figure 5.15: Tip displacement (cm) from both the full order model and the reduced order model for a streamlined tail setup vs time (s) with U=4 m/s. The reduced order model shows the cylinder will flutter by the amplitude of the tip displacement diverging non-monotonically

There was again good agreement between the reduced order model, the full-order model, and experiments for a streamlined tail. In the reduced order model flutter forms abruptly, but the full order model shows flutter slowly forming from divergence. The general trends are still in agreement because both models predict that first divergence develops and then becomes flutter at higher speeds. This is also in accordance with experimental observations by Paidoussis (Paidoussis, 2004). The major differences between the models is that the full-order model is able to predict amplitude of the instabilities and the reduced order model is only able to predict the existence of an instability. After performing the simulations, the following conclusions can be drawn:

- There is agreement between reduced order model and the full order model on the instability type for both the blunt end and the streamlined end. The results are summarized in Table 5.1.
- Cylinders with blunt tails are more stable than cylinders with streamlined tails.
- The reduced order model is able to accurately predict if and which instability the cylinder would experience. The reduced order model cannot predict the existence of limit cycles because it is a linear model. Therefore, if the amplitude of the instability is of interest to the researcher then the full order model is required.
- When the reduced order model predicts the cylinder is stable, it is unnecessary to run the full order model because they will both return results of near zero displacement.
- The time required to perform a reduced order simulation is orders of magnitude faster than the full order model used herein.

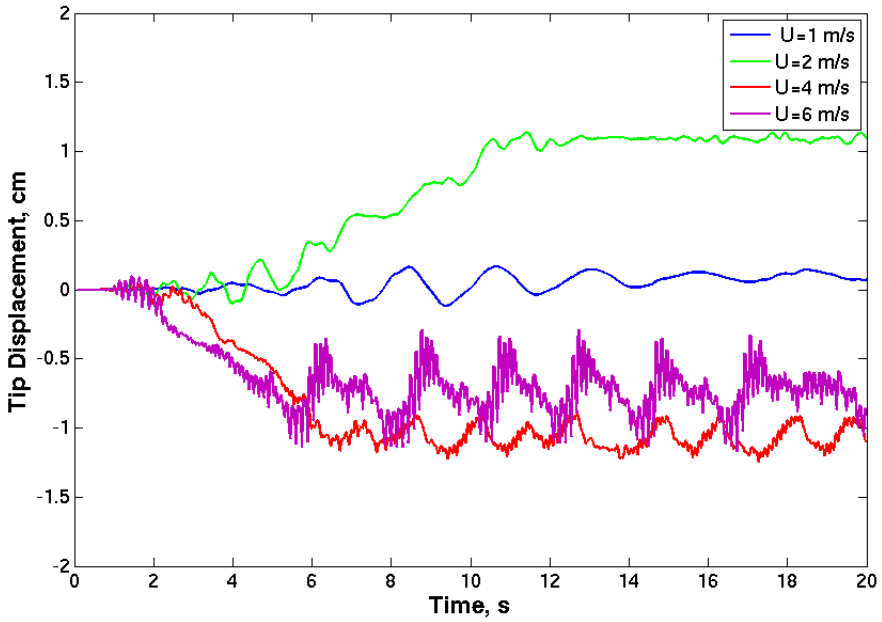

Figure 5.16: Tip displacement (cm) from the full order model for a streamlined tail setup vs time (s) with U=1,2,4,6 m/s.

Table 5.1: A recap of the results of all the comparison cases performed.

	Blunt end			Streamlined end		
	Experiment	ROM	FOM	Experiment	ROM	FOM
1 m/s	Stable	Stable	Stable	Stable	Stable	Stable
2 m/s	Stable	Stable	Stable	Diverge	Diverge	Diverge
4 m/s	Stable	Stable	Stable	Diverge	Diverge	Diverge
6 m/s	Stable	Stable	Stable	Flutter	Flutter	Flutter

Chapter 6
Conclusions

6.1 Summary of Work Performed

In this thesis two different models for a cylinder in axial flow were compared. The first was the Paidoussis model. It required formulating the governing equation into weak form and then implementing into a custom finite element program. The computer program written to solve the Paidoussis equation was written using the open source finite element library deal.ii, and was rigorously verified by using the method of manufactured solutions. This model coupled the incompressible Navier-Stokes equations for the fluid with an elastic model for the solid. The second model was implemented using OpenFOAM for the fluid domain and an in-house finite element solver called FEANL for the solid. These were coupled using an in-house coupling algorithm. The contribution of this work was to provide further evidence for the Paidoussis model to predict instability of elastic cylinders in axial flow.

This thesis highlights the strengths and weaknesses of both modeling approaches. The strength of the Paidoussis model is that it is a linear differential equation. This allows it to be implemented and run very quickly. This gives it the ability to quickly return results on predictions of instabilities. However, the Paidoussis strength is also its weakness. By being a linear equation, the Paidoussis model is not able to predict non-linear effects such as limit cycles.

On the other hand, the ability to predict non-linear phenomenon such as limit-cycle amplitude is one of the strengths of the full order model. The price of using these non-linear equations is a significantly higher cost in computational resources.

This is due to non-linear equations being much more difficult to solve. A recap of the work completed in this thesis is provided below.

1. A finite element program to solve the Paidoussis equation.
2. The method of manufactured solutions was used to verify the correct implementation of the reduced order model.
3. The energy of the system for the Paidoussis model was calculated for two different time stepping schemes.
4. Simulations of a cylinder in axial flow using a full order solver were performed.
5. The stability predictions of both models were compared.

6.2 Future Work

There is more than one way to create a reduced-order model. In this thesis, the reduced-order model made assumptions about the physics being modelled. These assumptions were then used to make simplifications to the governing equations and reduce them down to a linear equation. But this comes at a price; making assumptions can lead to losing the effects of important physics, and brings into question the validity of the assumptions being made.

Another approach to creating a reduced-order model (ROM) is by taking snapshots of the solution from the full-order model. A statistical method is then applied to the set of snapshots to derive a basis for the system's response that is "optimal" in some sense. By perturbing the conditions used to create the ROM, it can be used to simulate different conditions.

This statistical or empirical approach to ROM creation has the advantage of being devised from first principles. It can be thought of as being a method for mathematically choosing which physics are to be left out of the model. The major advantage of using an empirical reduced order model is that they still retain of the non-linearity of the original governing equations. This captures some non-linear effects such as limit cycles. This is in contrast to making educated guesses on what assumptions to make so that the governing equations can be simplified. Both methods have their strengths and weakness. Empirical ROMs are typically more

accurate but take longer to run and have smaller ranges of validity. Reduced-order models devised by making assumptions of the underlying physics, might not offer the same accuracy of the empirical ROM but can often be computed faster. To the author's knowledge no towed array empirical ROMs exist.

One problem with empirical ROMs is that they are very specific to the conditions used to create them; i.e. the domain, flow conditions etc. This leads to ROMs unable to handle large deformations because of change to the domain. Unfortunately, towed arrays can have large deformations and it would be prohibitively expensive to produce a ROM for all the possible configurations the array can deform into.

I propose overcoming this deficiency by using a combination of domain decomposition and proper orthogonal decomposition to create a database of "ROM Elements" that can be assembled and coupled into complicated configurations. By dynamically updating the elements as the structure deforms, I hope to be able to handle large deformations in fluid-structure interaction problems. My idea is similar to the finite element method. Finite elements decompose the domain into a number of elements where the governing equations are solved for each element. This technique will be similar in that the domain will be broken up into elements, but the shape function for the element will be a velocity field throughout the domain. In essence, it's creating a very large set of reduced order models by assembling reduced order models from a much smaller set of generator reduced-order models. By utilizing a much smaller generator set, the computation and memory requirements should be significantly reduced. To keep the generator set small, the simple geometry of a towed array will utilized.

I plan on applying this technique to model a cylinder in axial flow. To the best of my knowledge, all reduced-order modelling techniques for a cylinder in axial flow have consisted of making assumptions on the physics. There have been no attempts to apply a statistical approach to creating a reduced-order model for a cylinder in axial flow.

Appendix A
Non Technical Abstract

Computer simulations are playing an increasingly important role in the design process for engineers. This has lead to a demand to be able to simulate complex systems with a high level of accuracy. Advances in computer hardware has greatly increased our computational abilities over the years. Problems that used to be too computationally expensive can now be routinely solved by simply applying a lot of computing power.

The successful application of computer simulation to engineering has resulted in a demand for accurate solutions at a fraction of the time. To answer that problem, researchers have developed reduced order models by making assumptions on which physics of the problem are dominating. The assumptions, simplify the governing equations the computer has to solve, and results in simulations that run orders of magnitude faster. The computational savings come at a price. The price being that the reduced order model does not capture all the physics of the problem. Therefore, it is of absolute importance to know under what situations the unmodeled physics have little effect so that a reduced order model can be used to gain a computational savings.

This thesis focuses on comparing a first-principles fluid-structure interaction solver and a reduced order model. A fluid-structure interaction problem was chosen because of the high computational cost that is associated with that type of multi-physics problem. The full order model solves the incompressible Navier-Stokes equations for the fluid and elasticity equations for the solid. The reduced order

model chosen for comparison in the thesis is the Paidoussis model for a cylinder in axial flow. The free stream velocity was varied for a cylinder with a blunt tail and for a streamlined tail. The results were then compared to the predictions by the full order solver.

Bibliography

C. Ablow and S. Schechter. Numerical simulation of undersea cable dynamics. *Ocean Engineering*, 10(6):443 – 457, 1983.

W. Bangerth, T. Heister, L. Heltai, G. Kanschat, M. Kronbichler, M. Maier, B. Turcksin, and T. D. Young. The `deal.ii` library, version 8.1. 1:1, 2013.

A. Barbagelata, P. Guerini, and L. Troiana. Thirty years of towed arrays at NURC. *Oceanography*, 21, No2:24–33, 2008.

Y. Bazilevs, V. Calo, T. Hughes, and Y. Zhang. Isogeometric fluid-structure interaction: theory, algorithms, and computations. *Computational Mechanics*, 43 (1):3–37, 2008.

Y. Bazilevs, M.-C. Hsu, J. Kiendl, R. Wüchner, and K.-U. Bletzinger. 3d simulation of wind turbine rotors at full scale. part ii: Fluid–structure interaction modeling with composite blades. *International Journal for Numerical Methods in Fluids*, 65(1-3):236–253, 2011. ISSN 1097-0363.

S. Bhattacharyya, C. Vendhan, and K. Sudarsan. The finite element method for hydroelastic instability of underwater towed cylindrical structures. *Journal of Sound and Vibration*, 237(1):119 – 143, 2000. ISSN 0022-460X.

R. D. Blevins. *Applied Fluid Dynamics Handbook*. Van Nostrand Reinhold Company, 1984.

S. C. Brenner and L. R. Scott. *The Mathematical Theory of Finite Element Methods*. Spring, 2002.

D. Calkins. A metamodel-based towed system simulation. *Ocean Engineering*, 26 (11):1183 – 1247, 1999. ISSN 0029-8018.

R. L. Campbell and E. G. Paterson. Fluid–structure interaction analysis of flexible turbomachinery. *Journal of Fluids and Structures*, 27(8):1376–1391, 2011.

R. H. C.C. Ni. An experimental study of the flow-induced motions of a flexible cylinder in axial flow. *Journal of Fluids Engineering*, 100:389–394, 1978.

D. Chapman. Towed cable behaviour during ship turning manoeuvers. *Ocean Engineering*, 11(4):327 – 361, 1984. ISSN 0029-8018.

Y. Chen and M. Weber. Flow-induced vibrations in tube bundle heat exchangers with cross and parallel flow. In *ASME Symposium on Flow Induced Vibrations in Heat Exchangers, ed., DD Reiff*, pages 57–77, 1970.

E. De Langre, M. P. Paidoussis, O. Doare, and Y. Modarres-Sadeghi. Flutter of long flexible cylinders in axial flow. *Journal of Fluid Mechanics*, 571:371–389, 0 2007. ISSN 1469-7645.

J. Donea, S. Giuliani, and J.-P. Halleux. *An arbitrary lagrangian-eulerian finite element method for transient dynamic fluid-structure interactions*. Computer Methods in Applied Mechanics and Engineering, 1982. ISSN 0045-7825.

A. P. Dowling. The dynamics of towed flexible cylinders part 1. neutrally buoyant elements. *Journal of Fluid Mechanics*, 187:507–532, 1 1988. ISSN 1469-7645.

K. Dumont, J. Vierendeels, R. Kaminsky, G. Van Nooten, P. Verdonck, and D. Bluestein. Comparison of the hemodynamic and thrombogenic performance of two bileaflet mechanical heart valves using a cfd/fsi model. *Journal of biomechanical engineering*, 129(4):558–565, 2007.

J. Gagnon and M. Paidoussis. Fluid coupling characteristics and vibration of cylinder cluster in axial flow. part ii: Experiments. *Journal of Fluids and Structures*, 8(3):293 – 324, 1994a. ISSN 0889-9746.

J. Gagnon and M. Paidoussis. Fluid coupling characteristics and vibration of cylinder cluster in axial flow. part i: Theory. *Journal of Fluids and Structures*, 8 (3):257 – 291, 1994b. ISSN 0889-9746.

P. Gerstoft, W. S. Hodgkiss, W. Kuperman, H. Song, M. Siderius, and P. L. Nielsen. Adaptive beamforming of a towed array during a turn. *Oceanic Engineering, IEEE Journal of*, 28(1):44–54, 2003.

J. Gobat and M. Grosenbaugh. Whoi cable: time domain numerical modeling of moored and towed oceanographic systems. In *OCEANS '98 Conference Proceedings*, volume 3, pages 1681–1685 vol.3, 1998.

J. Gobat and M. Grosenbaugh. Time-domain numerical simulation of ocean cable structures. *Ocean Engineering*, 33(10):1373 – 1400, 2006. ISSN 0029-8018.

K. Gogan. The sounds of the sea: Marione acoustics, April 2014.

M. A. Grosenbaugh. Transient behavior of towed cable systems during ship turning maneuvers. *Ocean Engineering*, 34(11-12):1532 – 1542, 2007. ISSN 0029-8018.

C. C. G.S. Traintafyllou. The dynamics of towed arrays. *Offshore Mech. Arct. Eng*, 111:6, 1989.

W. R. Hawthorne. The early development of the dracone flexible barge. *Proceedings of the Institution of Mechanical Engineers*, 175(1):52–83, 1961.

S. Hopland. Investigation of cable behaviour in water during laying of fiberoptic submarine cables. In *Proc. International Wire and Cable Symposium*, pages 734–39, 1993.

R. Issa. Solution of the implicitly discretized fluid flow equations by operator splitting. *Journal of Computational Physics*, 62:6, 1989.

H. Jasak. *Error analysis and estimation for the finite volume method with applications to fluid flows*. PhD thesis, Imperial College London (University of London), 1996.

A. O. Katsuhisa Fujita. Effect of structural dimensions on dynamic stability of elastic beam subject to axial flow in confined narrow passage. *System Design and Dynamics*, 4:809–822, 2010.

M. Kheiri, M. Païdoussis, M. Amabili, and B. Epureanu. Three-dimensional dynamics of long pipes towed underwater. part 1: The equations of motion. *Ocean Engineering*, 00(0):0– 0, 2013. ISSN 0029-8018.

C. Kopp. Identification underwater with towed array sonar. In *Pacifici Maritime Conference*, 2010.

U. Kuttler, C. Forster, and W. A. Wall. A solution for the incompressibility dilemma in partitioned fluid–structure interaction with pure dirichlet fluid domains. *Computational Mechanics*, 38(4-5):417–429, 2006.

M. Lasky, R. Doolittle, B. Simmons, and S. Lemon. Recent progress in towed hydrophone array research. *Oceanic Engineering, IEEE Journal of*, 29(2):374 – 387, april 2004. ISSN 0364-9059.

S. G. Lemon. Towed-array history, 1917-2003. *IEEE Journal of Oceanic Engineering*, 29:365–373, 2004.

M. J. Lighthill. Note on the swimming of slender fish. *Journal of Fluid Mechanics*, 9:305–317, 9 1960. ISSN 1469-7645.

Z. Liu, Y. Liu, and J. Lu. Fluid-structure interaction of single flexible cylinder in axial flow. *Computers & Fluids*, 56(0):143 – 151, 2012. ISSN 0045-7930.

F. Lu, E. Milios, S. Stergiopoulos, and A. Dhanantwari. New towed-array shape-estimation scheme for real-time sonar systems. *Oceanic Engineering, IEEE Journal of*, 28(3):552 – 563, july 2003. ISSN 0364-9059.

A. Masud and T. J. Hughes. A space-time galerkin/least-squares finite element formulation of the navier-stokes equations for moving domain problems. *Computer Methods in Applied Mechanics and Engineering*, 146(1):91–126, 1997.

H. G. Matthies and J. Steindorf. Partitioned strong coupling algorithms for fluid–structure interaction. *Computers & Structures*, 81(8):805–812, 2003.

C. Michler, S. Hulshoff, E. Van Brummelen, and R. De Borst. A monolithic approach to fluid–structure interaction. *Computers & fluids*, 33(5):839–848, 2004.

F. Milinazzo, M. Wilkie, and S. Latchman. An efficient algorithm for simulating the dynamics of towed cable systems. *Ocean Engineering*, 14(6):513 – 526, 1987. ISSN 0029-8018.

S. T. Miller, R. Campbell, C. Elsworth, J. Pitt, and D. Boger. An overset grid method for fluid-structure interaction. *World Journal of Mechanics*, 2014, 2014.

M. Obligado and M. Bourgoin. An experimental investigation of the equilibrium and stability of long towed cable systems. *New Journal of Physics*, 15(4):043019, 2013.

Orcina. Orcaflex manual version 9.8a.

M. Païdoussis. *Dynamics of submerged towed cylinders*. McGill University, Mechanical Engineering Research Laboratories, 1970.

M. Paidoussis. Dynamics of cylindrical structures subjected to axial flow. *Journal of Sound and Vibration*, 29(3):365 – 385, 1973.

M. P. Paidoussis. Stability of towed, totally submerged flexible cylinders. *Journal of Fluid Mechanics*, 34:273–297, 10 1968.

M. P. Paidoussis. *Fluid-Structure Interactions Slender Structures and Axial Flow Volume 2*. Elsevier Academic Press, 2004.

H. Park, D. Jung, and W. Koterayama. A numerical and experimental study on dynamics of a towed low tension cable. *Applied Ocean Research*, 25(5):289 – 299, 2003.

J. Pike. Towed array. *http://www.globalsecurity.org*, March 2013.

J. Potter, E. Delaory, S. Constantin, and S. Badiu. The a lightweight, ultra-thin (8 mm od) towed array for use from small vessels of opportunity. In *Underwater Technology, 2000. UT 00. Proceedings of the 2000 International Symposium on*, pages 49 –53, 2000.

P. Roache. *Verification and Validation in Computational Science and Engineering*. Hermosa Publishers, 1998.

K. Singh, S. Michelin, and E. De Langre. The effect of non-uniform damping on flutter in axial flow and energy-harvesting strategies. *Proceedings of the Royal Society A: Mathematical, Physical and Engineering Science*, 468(2147):3620–3635, 2012.

S. Srivastava and C. Ganapathy. Experimental investigations on loop manoeuvre of underwater towed cable-array system. *Ocean Engineering*, 25(1):85 – 102, 1998.

S. Turek and J. Hron. Proposal for numerical benchmarking of fluid-structure interaction between an elastic object and laminar incompressible flow. In H.-J. Bungartz and M. Schäfer, editors, *Fluid-Structure Interaction*, volume 53 of *Lecture Notes in Computational Science and Engineering*, pages 371–385. Springer Berlin Heidelberg, 2006. ISBN 978-3-540-34595-4.

M. Vaz and M. Patel. Transient behaviour of towed marine cables in two dimensions. *Applied Ocean Research*, 17(3):143 – 153, 1995. ISSN 0141-1187.

M. T. Vineet Kumar Srivastava, YVSS Sanyasiraju. Dynamic behavior of underwater towed-cable in linear profile. *International Journal of Scientific & Engineering Researc*, 2:9, July 2011.

M. Zhdanov. 3D inversion of towed streamer EM data: A model study of the Harding field and comparison to 3D CSEM inversion, SEG Exhibition, September 2011.